Photoinduced processes in dye-sensitized photoanodes under the spotlight: a multiscale in silico investigation

Menzel, J.P.

CHAPTER 4

Photoinduced Electron Injection in a Fully Solvated Dye-Sensitized Photoanode: A Dynamical Semi-Empirical Study

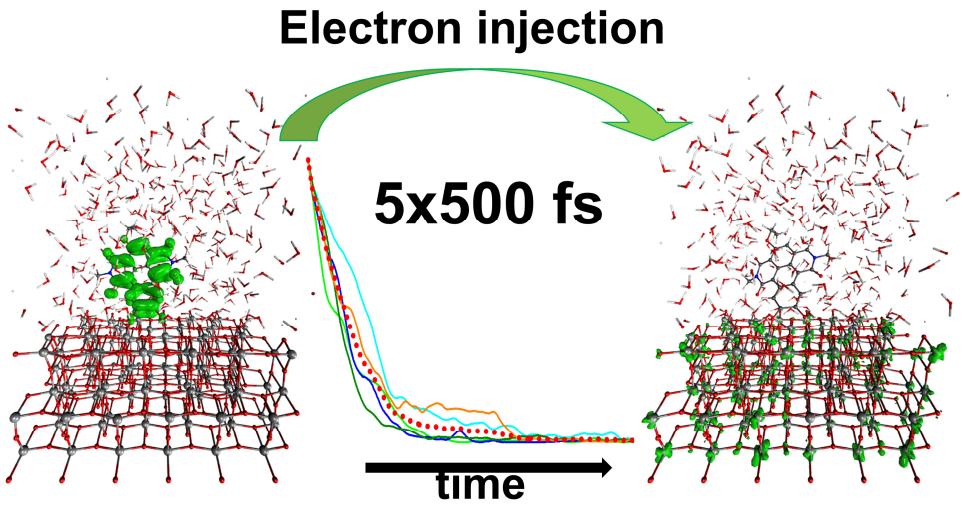

This Chapter is based on:

Jan Paul Menzel, Anastasios Papadopoulos, Jelena Belić, Huub J.M. de Groot, Lucas Visscher, Francesco Buda; *Journal of Physical Chemistry C*, **2020**, *124*, 27965-27976

4

ABSTRACT

Dye Sensitized Solar Cells (DSSCs) and Dye Sensitized Photoelectrochemical Cells (DS-PECs) have attracted much interest in recent years for solar energy conversion. More effort is still required to increase the efficiency of these devices, which is closely linked to the crucial process of photoinduced charge separation. Computational studies can provide insight into this fundamental process and suggest molecular components and interfaces that feature optimal energy level alignment before time consuming trial-and-error experimental realization. Here, we use a combination of Density Functional based Tight Binding (DFTB) and an extended Hückel approach to perform quantum-classical simulations of photoinduced electron injection in a TiO_2 Dye-Sensitized Photoanode with explicit solvation at a reasonable computational cost. In particular, we evaluate injection capabilities of core extended Napthalene Diimide (NDI) dyes with three different anchoring groups. Our results stress the importance of nuclear motion as well as conformational and trajectory sampling for a realistic description of the injection process. Furthermore, explicit solvation highly influences the conformational space explored by the dye and anchoring molecules, especially concerning the adsorption mode. Taking these effects into account, the core extended NDI with a catechol based anchoring moiety shows to be the most promising ultrafast electron injector. Our strategy allows for a more systematic computational search for appropriate molecular chromophores in dye-sensitized devices for solar energy conversion.

4.1 Introduction

In the search for environmentally friendly, renewable energy sources, Dye-Sensitized Solar Cells (DSSCs) have a high potential as a cost-effective alternative to silicon based photovoltaic cells in solar energy conversion.[1–3] These devices consist of semiconductor-based electrodes, which have been sensitized with photoactive molecular chromophores that absorb in the visible light range. DSSCs can also be extended by including molecular catalysts for direct conversion of solar energy to chemical fuel (Dye-Sensitized Photoelectrochemical Cells or DS-PECs). Both of these devices have attracted continued scientific interest.[4–8]

The anode or the cathode can be dye-sensitized to activate redox processes in the two half-cells. In this work we will focus on the design of a dye-sensitized photoanode, with a schematic set-up shown in figure 4.1. A semiconductor electrode (here TiO_2) is sensitized with a molecular dye (here a core extended NDI). The dye is attached via an anchoring group (here catechol).

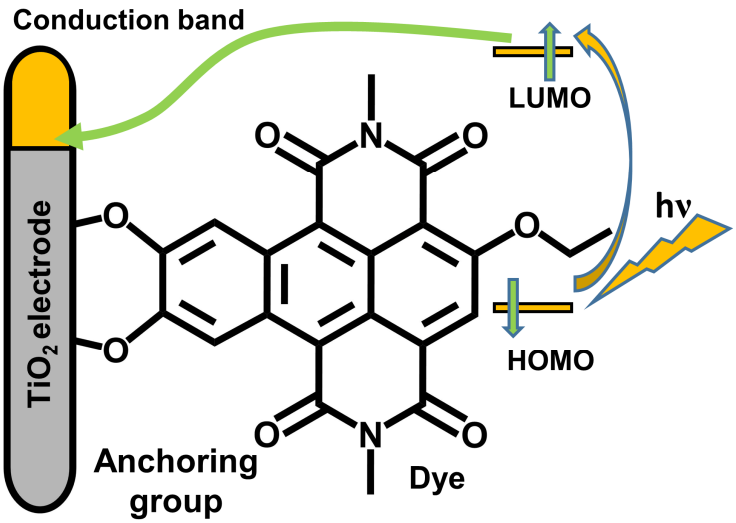

Figure 4.1. Characteristic set-up of a dye-sensitized photoanode: a dye molecule is attached via an anchoring group to a semiconductor electrode. Upon photoexcitation to the LUMO, the dye injects an electron into the conduction band of the semiconductor.

Upon photoexcitation with visible light, the excited electron is injected from the dye's LUMO into the conduction band of the electrode. This electron is then transferred via an external circuit towards the cathode. In DSSCs, electron flow from the cathode towards the anode via the electrolyte is then carried by redox mediators, which pick up the electron, diffuse towards the anode and reduce the photooxidized dye, completing the cycle. In the case of DS-PECs, the photooxidized dye is regenerated by electrons extracted from water splitting via a suitable water oxidation catalyst (WOC), generating oxygen and protons in the process. The protons diffuse via a proton exchange membrane (PEM) towards the cathode, where, in combination with the electron, the chemical fuel is produced, *e.g.* hydrogen from proton reduction or carbon based fuel from CO_2 reduction.[9]

For both types of devices (DSSCs and DS-PECs), the energetic alignment of the involved electronic states is absolutely crucial for obtaining a high forward reaction yield. The thermodynamic driving force and the electronic coupling between the molecular excited state and the semiconductor conduction band need to be tailored for rapid electron injection from the dye into the electrode, while suppressing wasteful back transfer and charge recombination.[10,11] To find a good compromise between these two contrasting but related requirements remains challenging.

Computational chemistry can provide insight into specific fundamental processes involved, such as interfacial electron transfer and charge separation.[12,13] It can deliver tools to screen through potential molecular dyes and interfaces to propose candidates before time consuming synthesis and tedious experimental investigations.[14] Density Functional Theory (DFT) based methods are often used to compare orbital energies of the molecular dyes with the electrodes' conduction band states and localization of the involved frontier orbitals.[15–18] Unfortunately, limitations of standard exchange correlation functionals may hinder the comparison with experimental values. For isolated molecular dyes, Linear Response Time Dependent DFT (LR-TDDFT) gives much more reliable results.[19–21]

However, these static approaches cannot capture changes in the electronic wave functions as the molecular conformations change. In addition, delocalization and localization effects, as well as changing orbital character due to *e.g.* forming or breaking of conjugation are not described either. These effects can be included in a limited way by ensemble averaging, taking geometries from equilibrated molecular dynamics (MD) runs. However, changes in the geometry during the injection process itself remain elusive. Finally, interaction of different electronic states can turn out to provide a pathway dominating the injection process when the electronic system is propagated.

Real-time evolution of the photoexcited electron can provide important insight into the dynamic aspect of these ultrafast injection processes. Non-adiabatic molecular dynamics (NAMD) approaches would be a favorable method, since they include the coupling between electronic and nuclear dynamics, but in practice this is still very expensive to use in these extensive systems over long time scales.[22–26] Both surface hopping and Ehrenfest-type approaches based on (TD)DFT have been successfully used to simulate electron injection processes[27–31]. These methods are computationally demanding and thus strongly limited with respect to the size of the system that can be investigated, especially if one is interested in performing several trajectories and compare numerous dye-semiconductor systems and their respective performances.

An alternative, computationally very efficient route to simulate the electron injection from photoexcited dye molecules was put forward by Rego and Batista.[32] In this method, the photoinduced electron dynamics is modelled via quantum dynamics based on an extended Hückel Hamiltonian. The approach was first demonstrated with a simulation of photoinduced electron injection from catechol into a TiO_2 anode.[32] It has been successfully used to elucidate electron transfer processes in a range of systems, including TiO_2 based electrodes with organic dyes,[32–38] DSSCs with transition metal complex based sensitizers,[39–46] nanocrystals[47,48] and charge separation dynamics in metal complexes.[49,50] While in

earlier simulations using this approach, the electron dynamics was done on fixed nuclear geometries, later implementations included the use of precalculated nuclear trajectories to model the effect of nuclear dynamics on the electron injection process.[37,49,51] Within this efficient, semiclassical approach, switching between the adiabatic MO basis and the diabatic AO basis allows for nonadiabatic population transfer. More recently, this method has also been extended to use the nonadiabatic elements derived from the quantum mechanically treated electronic system as an additional force in the classical MD to allow for persistent change of the nuclear trajectory in response to the evolution of the electronic subsystem.[52–55]

Here, we investigate electron injection properties of an extended core Naphthalene Diimide (NDI) dye with different anchoring groups in a TiO_2 based-dye sensitized photoanode using a combination of Self Consistent Charge Density Functional Based Tight Binding (SCC-DFTB) for the nuclear dynamics and the before mentioned extended Hückel method for the electron transfer dynamics (ETD). The main goal is to give an overview of the relative importance of nuclear motion, influence of different initial conformations and trajectories as well as inclusion of explicit solvation. In particular, explicit solvation can have several different effects on the photoinduced electron injection process: (*i*) the solvent can change the absorption properties of the molecular dye, (*ii*) it has an influence on the configurational space explored specifically at the dye-electrode interface, (*iii*) water tends to coadsorb onto the semiconductor interface and polarize the surface, thereby changing the band structure and the energy of the surface states, (*iv*) the water can interact directly with the anchored dye via breaking bonds between anchor and electrode, or by forming hydrogen bonds.

We aim to determine the most appropriate anchoring group for our dye with respect to their electronic conductivity and injection properties. For this, three benzene – derived anchoring moieties were chosen: benzoic acid, catechol and benzohydroxamic acid. Carboxylic acids are probably the most widely used anchoring groups but lack chemical stability, catechol and benzohydroxamic acid

show reasonable chemical stability and high estimated electron injection capabilities.[56] The investigated anchoring molecules are shown in figure 4.2a-c.

As molecular photosensitizer, an NDI-based dye was used, as NDIs are powerful light absorbers. They have a high extinction coefficient and can be tuned over the entire visible light range by introduction of electron withdrawing- or donating groups.[14,57,58] In figure 4.2d-f, the investigated core extended ethoxy NDIs, with the anchoring moieties fused into the extended core, are shown, which will be named cat-NDI, ben-NDI and hyd-NDI, according to their respective anchoring group.

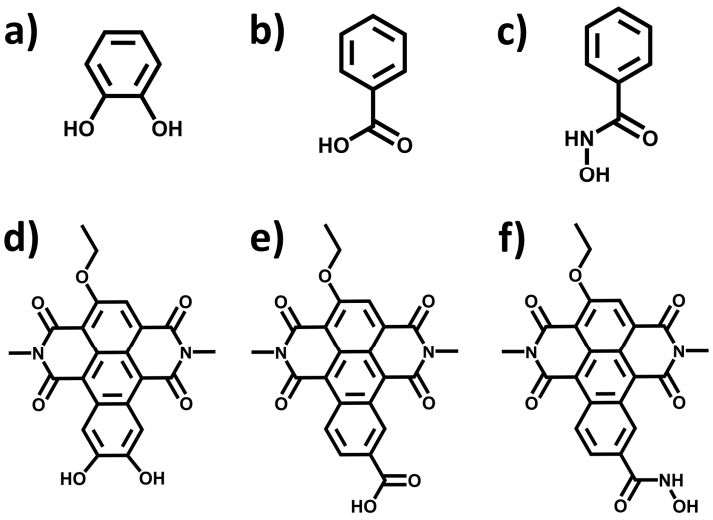

Figure 4.2. Investigated anchoring and dye molecules: **a)** catechol, **b)** benzoic acid, **c)** benzohydroxamic acid, **d)** core extended ethoxy-NDI with catechol anchoring group (cat-NDI), **e)** core extended ethoxy-NDI with carboxylic acid anchoring group (ben-NDI), **f)** core extended ethoxy-NDI with hydroxamic acid anchoring group (hyd-NDI).

The chapter is organized as follows: first, a description of the computational methods is given, which includes a short overview of the general procedure, the construction of the photoanode system *in silico*, treatment of the nuclear subsystem and finally the electron transfer dynamics. In the following section, we discuss our

results, with special focus on the effect of nuclear dynamics, trajectory averaging and explicit solvation. Conclusions are given in the last section.

4.2 Computational Methods

General Procedure

To evaluate the performance of the chosen dye and anchoring molecules, a quantum-classical semiempirical method is used, which allows for simulations of the full photoanode system at relatively low computational cost. Interfacial electron transfer simulations based on quantum dynamics using the AO/MO propagator and an extended Hückel Hamiltonian[50] are performed on *a priori* generated nuclear trajectories obtained at the SCC-DFTB-MD level.[59–61] The extended Hückel Hamiltonian is parametrized on DFT results (see section 4.A1 in the appendix for detailed information). The general workflow is described in scheme 4.1.

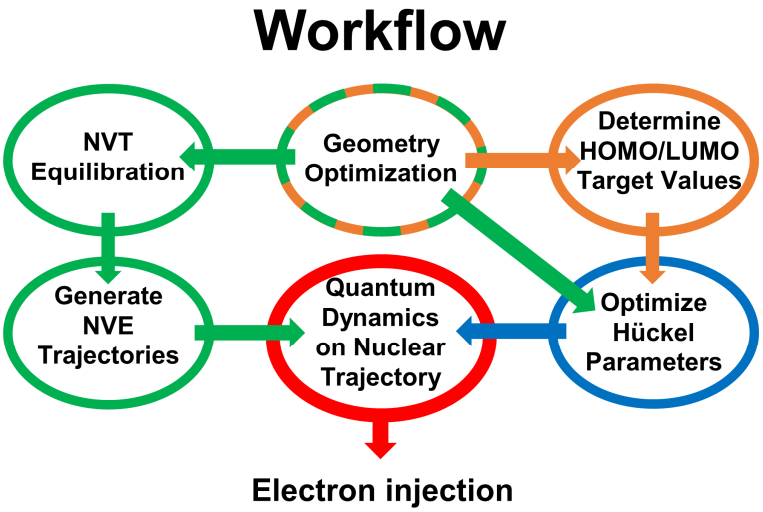

Scheme 4.1. Preparation of nuclear trajectories and extended Hückel parameters used in the semi-empirical quantum classical simulations of photoinduced electron injection. Colors refer to different computational methods: green for SCC-DFTB, orange for DFT/B3LYP, blue for Hückel parameter optimization, red for the AO/MO propagation using the extended Hückel Hamiltonian. DFT-based geometries are used for HOMO/LUMO target values determination, while DFTB-based geometries are used for the trajectory generation and for the parameter optimization.

The DFTB module of the Amsterdam Density Functional (ADF) program was used for simulating the nuclear dynamics (green box in Scheme 4.1).[62,63] The tiorg-0-1 parameter set, which is optimized to describe bulk Ti and TiO_2 as well as TiO_2 surfaces with and without organic adsorbants, was chosen for the SCC-DFTB.[64] The ADF program was also used for determining the DFT target values for the parameter optimization (orange box in Scheme 4.1). The ETD simulations were performed using the code developed by Rego and Batista (red circle in Scheme 4.1).[32]

Constructing the Photoanode

The TiO_2 was assumed to be in the anatase phase, since this phase is photocatalytically more active than rutile TiO_2 and most often used for photoelectrodes.[65] To model the TiO_2 anatase electrode, first a bulk optimization was performed using a supercell of 48 atoms in total (16 titanium atoms, 32 oxygen atoms) and periodic boundary conditions. The box size was optimized as well. The resulting geometry can be seen in figure 4.3.

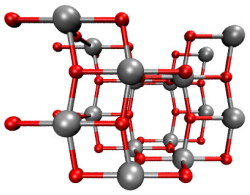

Figure 4.3. Optimized geometry of bulk anatase. Only one supercell is shown.

A supercell of 3 layers for a total of 144 atoms and cell dimensions of 10.045 Å x 15.234 Å x 70 Å with the surface normal into the *z* direction was used to model the anatase(101) surface starting from the optimized bulk geometry. The TiO_2 surface slab was reoptimized to model surface relaxation effects while the lowest layer was kept frozen in the bulk geometry. All anchoring groups were attached via bidentate bridging mode. The dissociating protons were adsorbed on the anatase surface to

keep the unit cell overall neutral. For the benzohydroxamic acid, the protonation state 1 was chosen (one proton is dissociated, one remains) as determined by Rudshteyn *et al.*[66] The optimized geometries of these anatase-anchor complexes are shown in figure 4.4.

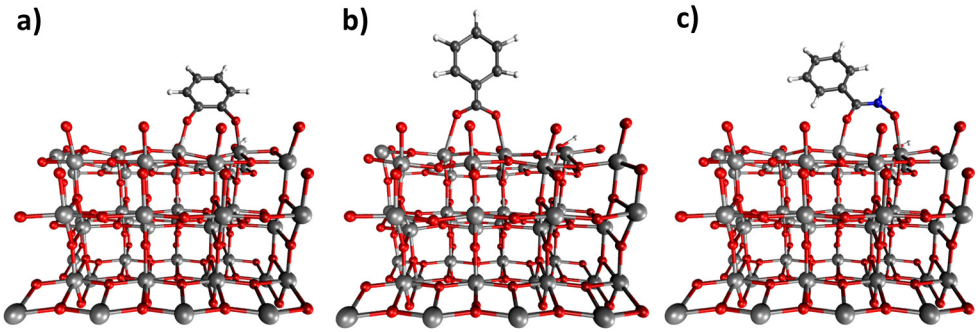

Figure 4.4. Optimized geometry of catechol **(a)**, benzoic acid **(b)** and benzohydroxamic acid **(c)** on anatase (101) surface.

Water molecules were added to obtain a total density of 1 g/ml. These water layers were constructed using a configuration extracted from bulk water equilibrated at 300K. Figure 4.5a shows this simulation box specifically for benzoic acid, containing a total of 453 atoms. SCC-DFTB based molecular dynamics simulations were performed while freezing the lowest TiO_2 layer to keep bulk geometry, as well as a layer of water on top to prevent evaporation. The simulation box for the ben-NDI, including a total of 1329 atoms and box dimensions of 20.091 Å x 22.851 Å x 70 Å is shown in figure 4.5b. Periodic boundary conditions are applied in all the directions. To avoid spurious interactions along the *z* direction, we add a vacuum layer of about 40 Å.

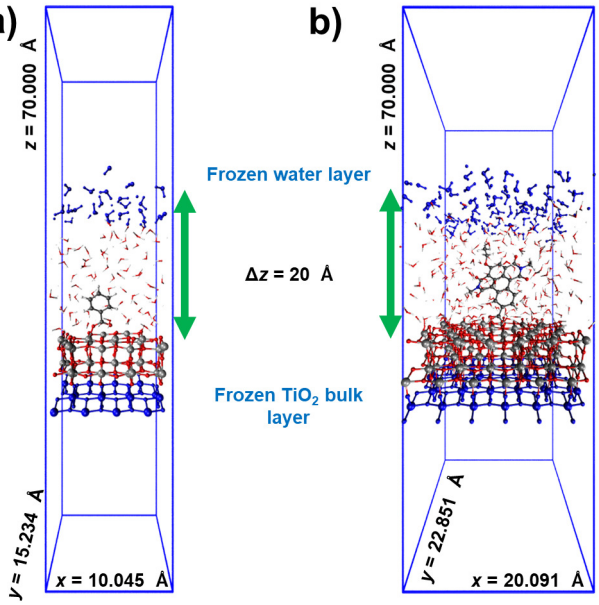

Figure 4.5. Simulation boxes for **a)** benzoic acid and **b)** ben-NDI attached to a TiO_2 -slab including explicit solvation. Periodic boundary conditions are enforced in *x*, *y* and *z*. Shown in blue are atoms kept frozen to mimic TiO_2 bulk geometry and to prevent evaporation and diffusion of the water molecules towards the opposite side of the TiO_2 slab.

Generating Nuclear Trajectories

In scheme 4.2, the general procedure to generate the nuclear trajectories is shown. First, a MD equilibration run in the NVT ensemble, using a Berendsen thermostat[67] at 300 K was performed for 5 ps with a time step of 1 fs. This was followed by a total of 1.5 ps in the NVE ensemble for the anchoring groups, while 2.5 ps were produced for the core extended NDI dyes. A time step of 0.1 fs was used for both. This short time step is necessary for stable ETD simulations. The resulting trajectory was then split into 15 parts of 100 fs each in the case of the anchoring groups. For the dyes, 5 slices of 500 fs each were taken. The initial geometries of these shorter trajectories were used for the ETD simulations on a fixed geometry.

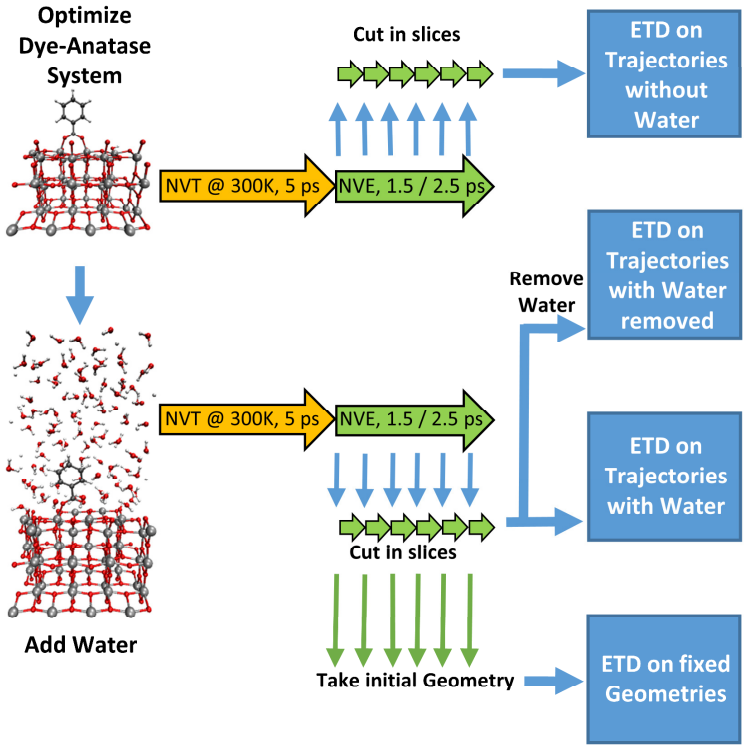

Scheme 4.2. Geometry and trajectory generation for usage in the ETD simulations. After an initial NVT equilibration at 300 K (yellow arrow), an NVE production run is performed (green arrow). This trajectory is then split into different slices for the quantum propagation. This procedure is performed twice, with and without explicit solvation. ETD simulations on static nuclear geometries were performed on the initial geometries of the trajectory slices.

To estimate the influence of explicit solvation, three different cases were investigated: (*i*) full explicit solvation during the nuclear trajectory generation and the ETD; (*ii*) the same nuclear trajectories but removing the water molecules for the ETD; (*iii*) nuclear trajectories and ETD without any water molecules. In this way, we can disentangle pure polarization effects due to the solvent from changes in the conformations explored during the dynamics, especially associated to formation of hydrogen bonds and changes of adsorption mode.

Electron Transfer Dynamics

The ETD simulations were performed using an extended Hückel Hamiltonian that is based on parametrization of Coulomb and overlap integrals. For the water molecules and anatase electrode the standard Hückel parameters were used.[68] The Hückel parameters for the dye and anchor molecules were optimized to achieve good relative energy alignment of the conduction band edge of the anatase on one hand and the frontier orbitals of the organic molecule on the other hand as determined by experimental values and DFT results. Consistent with the interpretation of the eigenvalues of the Hückel Hamiltonian as single particle energies, Hückel parameters were optimized on the dye and anchoring molecules in implicit water using ΔSCF derived values for the HOMO and ΔSCF plus excitation energy (TDDFT or experimental) for the LUMO energies at the DFT - B3LYP[69,70]/DZP[71] level with implicit COSMO[72] (Conductor-like Screening Model) water. A more detailed description and comparison to available experimental values is given in section 4A.1 in the appendix.

The excitation of each organic molecule is modelled by localizing the photoexcited electron on the LUMO of the corresponding adsorbed molecule, with the hole being localized at its HOMO. Even though there is evidence that catechol adsorbed to an anatase surface is excited directly to a charge transfer state with the electron already in the conduction band of the TiO_2,[73] the local excitonic state is used here, since we are interested in the ability of catechol to inject a photoexcited electron donated by an excited dye. We chose the same time step of 0.1 fs for nuclear and electronic propagation. This short time step is necessary for a stable ETD simulation since the time independence of the Hamiltonian during a nuclear time step is a reasonable approximation. The propagation is done for a total of 100 fs (anchoring molecules) or 500 fs (core extended NDIs). During the time evolution of the wave packets, the electron and hole population were calculated for the following fragments: the anatase electrode, the adsorbed organic molecule and the water molecules.

4.3 Results and Discussion

Nuclear Dynamics

During the equilibration dynamics with explicit solvent, water adsorption onto the anatase surface is observed in all systems considered in this work. Thereby, initial hydrogen bond formation towards the oxygen located on the surface steps (figure 4.6a) is followed by covalent attachment of the water oxygen to titanium (figure 4.6b). After adsorption, hydrogen bond formation to the surface oxygen, coadsorbed water molecules and bulk water is also common (see also 4.6b). These findings are consistent with work by Selli *et al*. and Aschauer *et al.* that found these geometries for multilayers of water on anatase(101).[74,75]

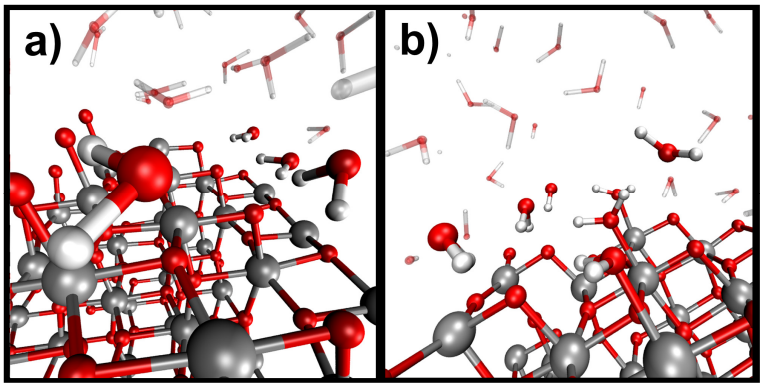

Figure 4.6. Adsorption of water on the anatase(101) surface: **a)** Initially, water molecules associate via hydrogen bonds to the oxygen on the surface step; the corresponding adsorbed water molecules are shown in ball and stick representation. **b)** Covalent bonds to Ti atoms are formed and hydrogen bonds to the bulk water create further water layers that remain relatively dynamic.

Interestingly, the adsorption mode of benzohydroxamic acid changes during the molecular dynamics. While the bidentate adsorption is most stable in vacuum, with explicit water it switches spontaneously to a monodentate mode with hydrogen bond formation to a coadsorbed water molecule. This happens via a water molecule in solution that attacks the oxygen-titanium bond by forming a hydrogen bond to the hydroxamic acid oxygen (figure 4.7a). Afterwards, the molecule rearranges to form a hydrogen bond to a neighboring adsorbed water molecule (see figure 4.7b). This

mode was also found to be the energetically most favorable with monolayer water present by Rudshteyn *et al.*[66] It is noteworthy that SCC-DFTB based MD is able to predict this correctly.

This change in adsorption mode from monodentate to bidentate is also present for ben-NDI and hyd-NDI. However, it also happens without explicit water, contrary to the benzohydroxamic acid. This change seems to be due to the steric stress of the imide part of the NDI that points towards the surface.

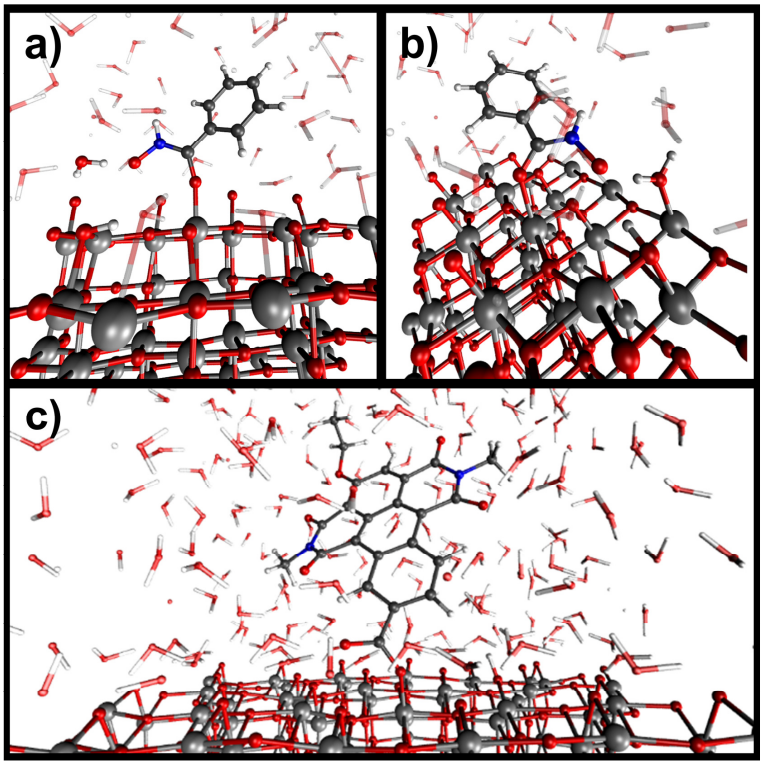

Figure 4.7. Change of the benzohydroxamic acid adsorption mode from bidentate to monodentate via **a)** attack of a water molecule (highlighted) and **b)** rearrangement forming a hydrogen bond to the highlighted coadsorbed water molecule; **c)** monodentate adsorption of ben-NDI due to steric stress induced by the imide part of the NDI pointing towards the surface.

This leads to angular strain on the anchoring group, that is released by breaking one of the bonds to the surface. An example is shown in figure 4.7c. In the case

without explicit water, the attractive interaction between the π-system and the anatase surface also plays a role, while the adsorbed water prevents this interaction when including explicit solvation. In the hyd-NDI case, this leads to π-stacking between the entire aromatic plane of the NDI and the surface.

Electron Injection Properties of Anchoring Molecules

The electron injection over time for one ETD simulation on a single trajectory with explicit solvation is given in figure 4.8a for the benzohydroxamic acid, where we show the electron population on different fragments over time.

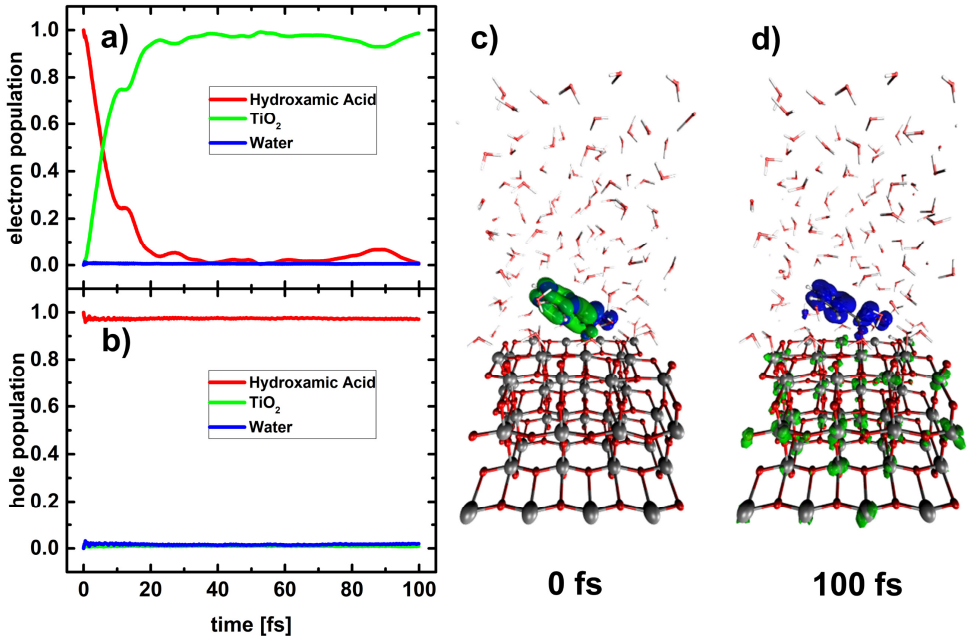

Figure 4.8. Electron **(a)** and hole **(b)** populations on the different fragments: Benzohydroxamic acid (red), TiO_2 (green) and water (blue) with full explicit solvation; **c)** electron (green) and hole (blue) density at the beginning of the simulation, both fully localized on the benzohydroxamic acid. **d)** electron (green) and hole (blue) density after 100fs. The electron is injected into the TiO_2 electrode, while the hole remains stable on the benzohydroxamic acid.

At the beginning of the simulation, both the hole and the electron are completely localized on the benzohydroxamic acid, occupying the respective HOMO and LUMO orbital (see figure 4.8c).

During the quantum dynamics evolution, the photoexcited electron is transferred from the benzohydroxamic acid to the anatase electrode. As can be seen, electron injection is complete within 20 fs (see figure 4.8a). No electron density is donated to the explicit water molecules. The hole population (see figure 4.8b) remains stable on the benzohydroxamic acid. At the end of the simulation, the electron is therefore injected into the electrode, while the hole remains on the benzohydroxamic acid: charge separation has occurred (see figure 4.8d).

However, one single trajectory can be misleading in drawing conclusions on the injection process. To obtain a reasonable estimate of the electron injection rate, several ETD results have to be averaged. In figure 4.9a, the photoinduced electron injection from the benzohydroxamic acid to the anatase electrode is averaged over all 15 ETD simulations performed on nuclear trajectories with explicit water. The same is shown for the hole in figure 4.9b.

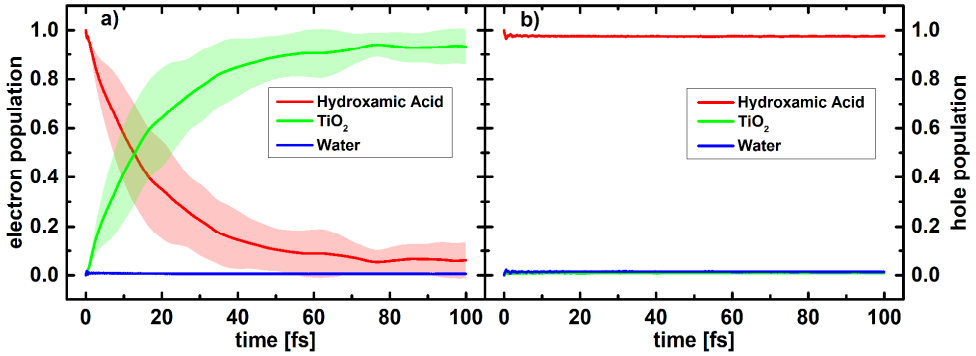

Figure 4.9. Electron **(a)** and hole **(b)** populations on the different fragments: Benzohydroxamic acid (red), TiO_2 (green) and water (blue) with full explicit solvation, averaged over 15 trajectories. The lines denote the mean values, the shaded area the standard deviation centered on the mean value.

Photoinduced electron injection is observed; however, the average rate is significantly lower than for the single trajectory discussed earlier: within about 60 fs on average, the injection is basically complete. This highlights the importance of appropriate statistics by averaging over multiple simulations in determining the injection rate. Some general statements can be made for all simulations and for all investigated molecules: (*i*) no significant electron population is observed on the water molecules, (*ii*) the hole remains stable on the organic molecule. Figures of electron and hole survival for all cases and molecules can be found in the appendix.

The importance of averaging over several geometries or trajectories is evident in figure 4.10a – 4.10d, where we report the electron injection evolution for each of the 15 geometries (4.10a) and trajectories (4.10c) of benzohydroxamic acid in explicit water, with the mean value and the standard deviation also included (figures 4.10b and 4.10d). Figure 4.10a shows that the choice of the initial geometry can lead to qualitatively different results: from almost no injection to a very fast process finished within 20 fs. Correspondingly, this leads to a high standard deviation and a slow, incomplete injection when considering the mean value, shown in figure 4.10b. We have analyzed in some more detail these different conformations to search for characteristic geometrical features that might affect the injection properties. While some features, such as a large dihedral angle between phenyl group and hydroxamic acid, as well as a large distance between anchoring group and TiO_2 often slow down the injection process, more complex collective geometric variables seem to be involved, not only including the chromophore but also the solvent and the semiconductor surface. It is therefore challenging to disentangle these features.

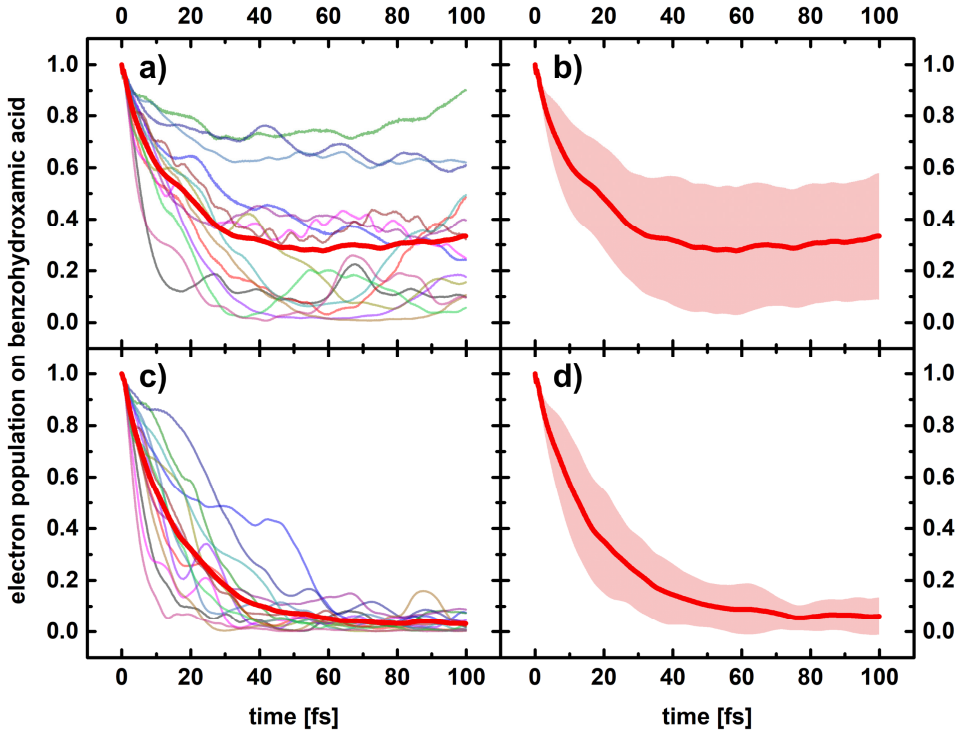

Figure 4.10. Variation of electron population on benzohydroxamic acid: **a)** all 15 ETDs on static geometries with the mean value in bold; **b)** the corresponding standard deviation (shaded area) centered on the mean value (bold line); **c)** all 15 ETDs on nuclear trajectories with the mean value in bold, **d)** the corresponding standard deviation (shaded area) centered on the mean value (bold line).

The effect of including dynamics is shown in figure 4.10c. Here, more geometries are explored during the trajectory and the rates change significantly compared to the static case. This means that if injection is hindered at a certain geometry, injection might be slowed down in the dynamic case, but not completely inhibited. For example, the value of the dihedral angle between anchoring group and aromatic system can prevent electron flow from the molecule to the anatase surface, but when a more favorable conformation is explored during the trajectory, the injection channel is opened (see a more detailed description in 4A.2). In previous investigations of photoinduced electron transfer processes, coherent effects between

nuclear and electronic motion have been shown to be relevant in facilitating the charge separation (see also chapter 3).[24,26,37,52] Here, we have also explored possible resonances between electronic and nuclear frequencies and show an example in section 4A.3 in the appendix. This suggests that the electronic system is able to take advantage of nuclear modes of appropriate frequency.

A further effect of the nuclear dynamics is the larger conformational sampling within the simulation leading to a significant decrease in the standard deviation (see figure 4.10d). The benzohydroxamic acid is the most extreme case, for the benzoic acid and catechol the variation between single ETD runs is significantly lower (see appendix 4A.4 and 4A.5).

The lower injection rate and large standard deviation of the static case is a consequence of the high variation between single trajectories and charge oscillations between surface and molecule visible in figure 4.10a. These oscillations are an effect of the finite size of the system that has been overcome in the past by including absorbing potentials in the lowest TiO_2 layer.[32,34,46] However, the oscillations are greatly reduced when including nuclear dynamics (see figure 4.10c), since dynamic disorder rapidly localizes the charge within the surface slab. This points to a sufficient size of our system without the need of using an artificial absorbing potential, as localized low energetic states are available through thermal noise in the TiO_2 slab. Since this is a dynamic effect within the electrode, the TiO_2 slab needs to be treated dynamically, as freezing the surface leads to the same oscillatory behavior observed in the completely static system (see figure 4A.10 in the appendix).

To check the relative importance of nuclear dynamics, trajectory averaging and explicit solvation on the electron injection process, we compare the average electron population over time on all three anchoring molecules for these different cases in figure 4.11. In all panels, only the electron population on the anchoring molecule averaged over all 15 ETDs is shown. Single runs and standard deviations are omitted for clarity and reported in the appendix (sections 4A.4 – 4A.6).

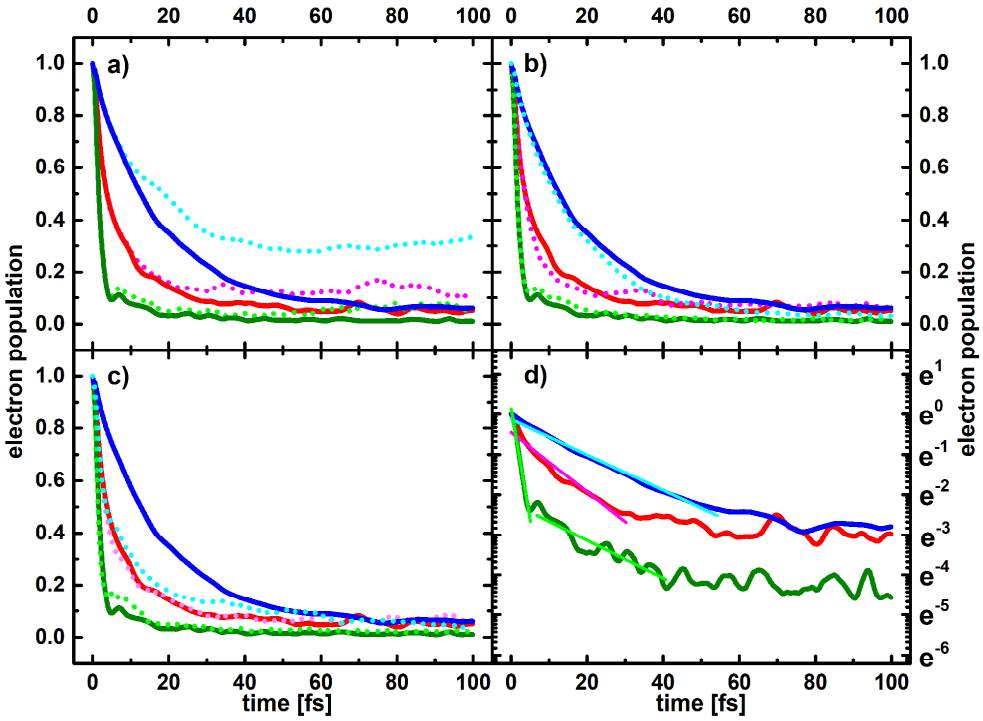

Figure 4.11. Electron population on catechol (red), benzoic acid (green) and benzohydroxamic acid (blue) averaged over 15 ETD simulations each. In different panels we compare the results obtained with the nuclear trajectories with explicit water (full lines) with the results obtained with **a)** static nuclear geometries (dotted lines), **b)** the same nuclear trajectories with the water molecules subsequently removed for the ETD (dotted lines), **c)** trajectories obtained without explicit solvation (dotted lines). Panel **d)** shows the electron injection for the fully solvated, dynamic case on a ln scale including a linear fit indicated in a lighter color.

In figure 4.11a, the average electron population over time on all three anchoring molecules are given for the static vs. the dynamic case. It is important to note that the geometries chosen are the initial structures from the trajectories (see scheme 4.2), meaning that the initial conditions for the static and dynamic cases are identical. The importance of nuclear dynamics for the description of the injection process is clearly visible. The electron injection is slower and less complete for all static cases in comparison to the dynamic ones due to larger differences in rate between single ETD

runs as well as oscillations between anchoring molecule and electrode. However, this effect varies by anchoring molecule. While for the benzoic acid especially the initial injection seems quite well described on static geometries, the difference between static geometries and nuclear trajectories is quite significant for catechol and very large for the benzohydroxamic acid. All in all, nuclear dynamics are quite important in the electron injection process. More conformations are explored during the trajectory, leading to smaller differences between single ETD runs. Conformations that inhibit electron injection do not prevent the process, as over time, other parts of conformational space are explored that allow for electron flow. Furthermore, dynamic disorder inhibits oscillations between the different fragments.

The importance of including explicit solvation is less straightforward. As mentioned earlier, to disentangle pure polarization effects from influence of the water on the conformational space explored, we investigated three cases: (*i*) nuclear trajectories obtained with full explicit solvation, (*ii*) the same trajectories but with the water molecules subsequently removed, thus keeping the effect on nuclear dynamics but removing polarization effects, and (*iii*) trajectories obtained in vacuum.

We first consider the pure polarization effect by comparing the ETDs of the full explicit solvation model and the same nuclear trajectories with the water molecules removed for the quantum dynamics, as given in figure 4.11b. For all three anchoring molecules, the difference between full explicit solvation and removing the water molecules for the ETD is quite small. The presence of the water slightly slows down the injection into the TiO_2 electrode for the benzohydroxamic acid, while the benzoic acid remains almost unchanged. For the catechol, injection without water is slightly increased at the beginning, but a small peak at 35 fs denotes minor back transfer that is suppressed when including explicit water. The differences decrease over the course of the simulation. We expect that the polarization effect is so small due to the tight binding character of the Hückel method, which poorly describes long range effects.

While the polarization effect of the water in our simulations is small, the effect of excluding water in the nuclear dynamics can be significant, as seen in figure 4.11c. While the conformational space explored with water seems to be very similar for catechol, as there is almost no difference in injection rate, this is not the case for the other two anchoring molecules. There is a quite clear back transfer peak after initial injection (at 5 fs) in the case of the benzoic acid that is significantly higher when excluding water. This can partially be explained by the missing polarization effects, as was the case in figure 4.10b, but is more pronounced and might hint at a lower dynamic disorder in the system. In both cases, full injection is achieved after about 40 fs. For the benzohydroxamic acid, the effect of explicit solvation is quite striking as the electron injection is a lot slower. This is most likely due to the changed adsorption mode discussed earlier, where the benzohydroxamic acid adsorbs bidentally in vacuum, but switches to monodentate adsorption mode when including explicit water (as was shown in figure 4.7). Explicit solvation therefore seems to be very important for the benzohydroxamic acid, less so for benzoic acid, and negligible for catechol. In addition, conformational differences induced by the water and direct interaction via formation of hydrogen bonds appear more important than polarization effects in this tight binding framework.

To compare injection rates for the three anchoring molecules, we give the electron population over time on a semi-logarithmic scale in figure 4.11d. Here we only focus on the fully solvated dynamic case. For all three anchoring molecules, the injection behavior seems to follow exponential behavior, until less than 10 % electron population remains on the dye. After that, noise takes over. A linear fit is given for this part of the electron injection plot, to estimate the rate. The slope, adjusted R^2 values, estimated rates and mean life time for the three anchoring molecules are given in table 4.1.

Table 4.1. Slope, adjusted R^2 values and estimated electron injection rates for catechol, the two regimes of the benzoic acid and the benzohydroxamic acid determined from the linear fits on the semi logarithmic mean value of 15 ETD simulations performed on fully solvated nuclear trajectories.

Molecule	Slope [fs^{-1}]	Adjusted R^2	Estimated Electron injection rate [s^{-1}]	Mean life time [fs]
Catechol	-0.074	0.95397	$7.4x10^{13}$	13.6
Benzoic Acid	-0.547	0.98888	$5.5x10^{14}$	1.8
	-0.048	0.87008	$4.8x10^{13}$	21.1
Benzohydroxamic Acid	-0.043	0.99302	$4.3x10^{13}$	22.8

The benzoic acid seems to have two distinct regimes: within the first 5 fs a very rapid injection, followed by a slower rate comparable to the other two anchoring groups. This is most likely a relaxation effect due to the strong coupling between TiO_2 surface states and the oxygens of the benzoic acid, as can be seen in the density of states (DOS) given in the appendix (figure 4A.2). The injection rates are all in the order of 10^{13} s^{-1}, with the first regime of the benzoic acid showing an even higher rate of the order of 10^{14} s^{-1}.

All in all, conformational averaging and inclusion of nuclear dynamics are crucial in describing the exponential decay of the injection process, while explicit solvation seems important for the correct description of nuclear dynamics, but not in the ETD simulations. While the injection rates vary when including or excluding nuclear dynamics and explicit solvation, the relative trend of the anchoring molecules stays the same.

Electron Injection Properties of Core-Extended NDI Dyes with Different Anchoring Groups

The electron injection properties of the excited anchoring molecules give some insight into the effects of nuclear motion and explicit solvation on these molecules as well as an estimate of their performance. In this section we focus on the electron injection properties of the whole photoanode system including the NDI based dyes shown in figure 4.2d-f.

A comparison of the average electron population over time on these NDI based dyes is given in figures 4.12a-d. Here we focus on the time evolution of the mean values averaged over 5 ETD simulations of 500 fs each. Figures with single trajectories and standard deviations can be found in the appendix (section 4A.7 to 4A.9). In figure 4.12a, we compare the electron injection evolution obtained with ETDs on static geometries with those performed on nuclear trajectories. Again, the geometries correspond to the initial structures of the trajectories, meaning that initial conditions are the same.

In general, electron injection here is significantly slower in comparison to the corresponding benzene derived anchoring molecules. This might be associated to both lower LUMO energies (and therefore lower driving force) and lower coupling of the molecules' LUMO to the conduction band states, as the distance between donor and acceptor is increased. While cat-NDI fully injects the photoexcited electron within 150 fs in the dynamic case, the exclusion of nuclear dynamics leads to a far lower injection with an electron population on the dye molecule of still 20 % after 500 fs. The same holds true for ben-NDI, where the electron population left on the dye rises from 10 % in the dynamic to approximately 50 % in the static case. For the hyd-NDI, this is even more striking: while the electron population on the dye is about 35 % after 500 fs when including nuclear dynamics, in the static case it actually rises from a minimum of 45 % at 300 fs to about 60 % after 500 fs.

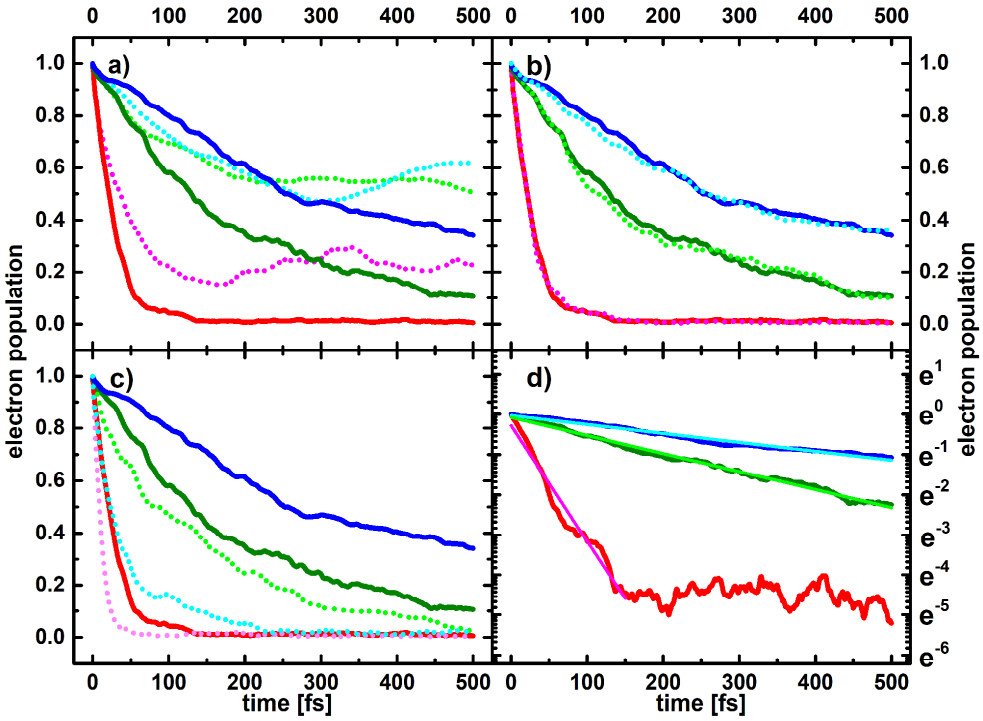

Figure 4.12. Electron population on cat-NDI (red), ben-NDI (green) and hyd-NDI (blue) averaged over 5 ETD simulations each. In different panels we compare the results obtained with the nuclear trajectories with explicit water (full lines) with the results obtained with **a)** static nuclear geometries (dotted lines), **b)** the same nuclear trajectories with the water molecules subsequently removed for the ETD (dotted lines), **c)** trajectories obtained without explicit solvation (dotted lines). Panel **d)** shows the electron injection for the fully solvated, dynamic case on a ln scale including a linear fit indicated in a lighter color.

Furthermore, the importance of explicit solvation in the trajectory generation is much more obvious here than for the benzene derivatives. While the removal of water molecules for the ETD leads to very little change (dotted lines in figure 4.12b in comparison to the full lines), the electron injection rate is significantly higher for all dye molecules when using nuclear trajectories obtained without explicit solvation (dotted lines in figure 4.12c). Interestingly, the trend of the injection properties changes also qualitatively. While in all cases, electron injection is quicker without explicit water, the hyd-NDI shows an extreme increase in injection rate and surpasses

the ben-NDI. This extreme change can be explained by the π-stacking of the hyd-NDI onto the surface that was mentioned earlier. Such an interaction leads to very strong electronic coupling between the NDI and TiO_2, that allows for direct injection between dye and surface without crossing the anchoring molecule (see figure 4.13). Consequently, it is absolutely crucial to include explicit solvation for the generation of nuclear trajectories to predict the performance of a molecular dye.

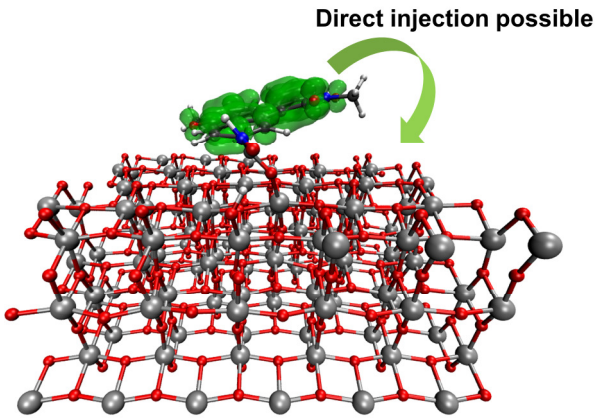

Figure 4.13. Representative geometry of hyd-NDI without explicit solvation. The close interaction between the π-system of the dye with the anatase surface allows for direct injection. The electron density (shown in green) does not need to pass through the anchoring moiety.

In figure 4.12d, the electron population on the core-extended NDI dyes averaged over 5 ETDs on trajectories with explicit water is shown on a semi-logarithmic scale. This allows for a linear fit to estimate injection rates. In comparison to the anchoring groups, the exponential behavior is even more evident. Slopes, adjusted R^2 values, estimated rates and mean survival time are given in table 4.2. The rates of injection are significantly lower than for the anchoring molecules. Still, the slowest injection (the hyd-NDI) has a mean life time of about 500fs, still 4-5 orders shorter than a typical fluorescence life time. The most effective anchor-dye complex is thus cat-NDI, which is one order of magnitude faster than the other two molecules. Ben-NDI

and hyd-NDI have comparable rates, with ben-NDI approximately twice as fast. Contrary to the benzene derived anchoring molecules, the catechol-based dye injects faster than the dye attached via a carboxylic acid group. This lower relative rate of the carboxylic acid integrated in the dye can be explained by the change of adsorption mode: while the benzoic acid stays in bidentate mode, the ben-NDI prefers monodental adsorption due to steric constraints, leading to a comparably lower injection rate.

Table 4.2. Slope, adjusted R^2 values and estimated electron injection rates for cat-NDI, ben-NDI and hyd-NDI determined from the linear fits on the semi logarithmic mean value of 5 ETD simulations performed on fully solvated nuclear trajectories.

Molecule	Slope [fs^{-1}]	Adjusted R^2	Estimated Electron injection rate [s^{-1}]	Mean life time [fs]
cat-NDI	-0.028	0.96446	$2.8x10^{13}$	35
ben-NDI	$-4.37x10^{-3}$	0.99203	$4.37x10^{12}$	224
hyd-NDI	$-2.21\ x10^{-3}$	0.97753	$2.21x10^{12}$	452

4.4 Conclusion

We have investigated the photoinduced electron injection from three different anchoring molecules (catechol, benzoic acid, benzohydroxamic acid) as well as from core extended NDI based dyes with these three anchoring moieties. An evaluation of the importance of nuclear dynamics, conformational averaging and explicit solvation for the injection process was done. Nuclear dynamics are crucial for describing the electron injection process, suppressing oscillations back to the dye molecules and localizing the electron through dynamic disorder. Conformational and trajectory averaging has a profound impact, especially in the benzoic acid and hydroxamic acid derivatives. This is further underlined by the fact that the injection rate is strongly dependent on the anchoring mode (bidentate bridging vs

monodentate). Explicit solvation is of importance regarding the correct adsorption mode of anchoring groups and correct overall dynamics of the dyes. This holds especially true for the hydroxamic acid. For the nuclear trajectory generation, explicit water should therefore be included. Explicit solvent polarization effects are low due to the tight binding character of the Hamiltonian. Concerning all anchor-dye complexes explored, the cat-NDI emerged as the most effective (full injection within 150 fs). The ben-NDI (with 90 % within 500 fs) and hyd-NDI (65 % within 500 fs) showed lower injection rates. The computational strategy employed, including the effect of nuclear dynamics, trajectory averaging and explicit solvation at a still reasonable computational cost, allows for a more unbiased screening of potential molecular dyes and may be relevant in the development of new dye sensitized photoanodes for solar energy conversion.

4.5 References

(1) O'Regan, B.; Grätzel, M. A Low-Cost, High-Efficiency Solar Cell Based on Dye-Sensitized Colloidal TiO 2 Films. *Nature* **1991**, *353*, 737–740.

(2) Cao, Y.; Saygili, Y.; Ummadisingu, A.; Teuscher, J.; Luo, J.; Pellet, N.; Giordano, F.; Zakeeruddin, S. M.; Moser, J.-E.; Freitag, M.; Hagfeldt, A.; Grätzel, M. 11% Efficiency Solid-State Dye-Sensitized Solar Cells with Copper(II/I) Hole Transport Materials. *Nature Communications* **2017**, *8*, 15390.

(3) Zhang, L.; Yang, X.; Wang, W.; Gurzadyan, G. G.; Li, J.; Li, X.; An, J.; Yu, Z.; Wang, H.; Cai, B.; et al. 13.6% Efficient Organic Dye-Sensitized Solar Cells by Minimizing Energy Losses of the Excited State. *ACS Energy Lett.* **2019**, *4*, 943–951.

(4) Hagfeldt, A.; Boschloo, G.; Sun, L.; Kloo, L.; Pettersson, H. Dye-Sensitized Solar Cells. *Chem. Rev.* **2010**, *110*, 6595–6663.

(5) Li, F.; Fan, K.; Xu, B.; Gabrielsson, E.; Daniel, Q.; Li, L.; Sun, L. Organic Dye-Sensitized Tandem Photoelectrochemical Cell for Light Driven Total Water Splitting. *J. Am. Chem. Soc.* **2015**, *137*, 9153–9159.

(6) Yamamoto, M.; Nishizawa, Y.; Chábera, P.; Li, F.; Pascher, T.; Sundström, V.; Sun, L.; Imahori, H. Visible Light-Driven Water Oxidation with a Subporphyrin Sensitizer and a Water Oxidation Catalyst. *Chem. Commun.* **2016**, *52*, 13702–13705.

(7) Jiang, J.; Spies, J. A.; Swierk, J. R.; Matula, A. J.; Regan, K. P.; Romano, N.; Brennan, B. J.; Crabtree, R. H.; Batista, V. S.; Schmuttenmaer, C. A.; Brudvig, G. W. Direct Interfacial Electron Transfer from High-Potential Porphyrins into Semiconductor Surfaces: A Comparison of Linkers and Anchoring Groups. *J. Phys. Chem. C* **2018**, *122*, 13529–13539.

(8) Massin, J.; Bräutigam, M.; Bold, S.; Wächtler, M.; Pavone, M.; Muñoz-García, A. B.; Dietzek, B.; Artero, V.; Chavarot-Kerlidou, M. Investigating Light-Driven Hole Injection and Hydrogen Evolution Catalysis at Dye-Sensitized NiO Photocathodes: A Combined Experimental–Theoretical Study. *J. Phys. Chem. C* **2019**, *123*, 17176–17184.

(9) Yu, Z.; Li, F.; Sun, L. Recent Advances in Dye-Sensitized Photoelectrochemical Cells for Solar Hydrogen Production Based on Molecular Components. *Energy Environ. Sci.* **2015**, *8*, 760–775.

(10) Haque, S. A.; Palomares, E.; Cho, B. M.; Green, A. N. M.; Hirata, N.; Klug, D. R.; Durrant, J. R. Charge Separation versus Recombination in Dye-Sensitized Nanocrystalline Solar Cells: The Minimization of Kinetic Redundancy. *J. Am. Chem. Soc.* **2005**, *127*, 3456–3462.

(11) Maggio, E.; Martsinovich, N.; Troisi, A. Evaluating Charge Recombination Rate in Dye-Sensitized Solar Cells from Electronic Structure Calculations. *J. Phys. Chem. C* **2012**, *116*, 7638–7649.

(12) Mai, S.; González, L. Molecular Photochemistry: Recent Developments in Theory. *Angewandte Chemie International Edition* **2020**, *59*, 16832–16846.

(13) Persico, M.; Granucci, G. Photochemistry. A Modern Theoretical Perspective.; Springer: Cham (Switzerland), 2018.

(14) Belić, J.; van Beek, B.; Menzel, J. P.; Buda, F.; Visscher, L. Systematic Computational Design and Optimization of Light Absorbing Dyes. *J. Phys. Chem. A* **2020**, *124*, 6380–6388.

(15) Le Bahers, T.; Labat, F.; Pauporté, T.; Lainé, P. P.; Ciofini, I. Theoretical Procedure for Optimizing Dye-Sensitized Solar Cells: From Electronic Structure to Photovoltaic Efficiency. *J. Am. Chem. Soc.* **2011**, *133*, 8005–8013.

(16) De Angelis, F.; Fantacci, S.; Selloni, A.; Grätzel, M.; Nazeeruddin, M. K. Influence of the Sensitizer Adsorption Mode on the Open-Circuit Potential of Dye-Sensitized Solar Cells. *Nano Lett.* **2007**, *7*, 3189–3195.

(17) Cheng, J.; Sulpizi, M.; Van de Vondele, J.; Sprik, M. Hole Localization and Thermochemistry of Oxidative Dehydrogenation of Aqueous Rutile TiO2(110). *ChemCatChem.* **2012**, *4*, 636–640.

(18) Yang, L.; Lindblad, R.; Gabrielsson, E.; Boschloo, G.; Rensmo, H.; Sun, L.; Hagfeldt, A.; Edvinsson, T.; Johansson, E. M. J. Experimental and Theoretical Investigation of the Function

of 4-Tert-Butyl Pyridine for Interface Energy Level Adjustment in Efficient Solid-State Dye-Sensitized Solar Cells. *ACS Appl. Mater. Interfaces* **2018**, *10*, 11572–11579.

(19) Pastore, M.; Mosconi, E.; De Angelis, F.; Grätzel, M. A Computational Investigation of Organic Dyes for Dye-Sensitized Solar Cells: Benchmark, Strategies, and Open Issues. *J. Phys. Chem. C* **2010**, *114*, 7205–7212.

(20) Pastore, M.; Fantacci, S.; De Angelis, F. Ab Initio Determination of Ground and Excited State Oxidation Potentials of Organic Chromophores for Dye-Sensitized Solar Cells. *J. Phys. Chem. C* **2010**, *114*, 22742–22750.

(21) De Angelis, F.; Fantacci, S.; Gebauer, R. Simulating Dye-Sensitized TiO2 Heterointerfaces in Explicit Solvent: Absorption Spectra, Energy Levels, and Dye Desorption. *J. Phys. Chem. Lett.* **2011**, *2*, 813–817.

(22) Akimov, A. V.; Neukirch, A. J.; Prezhdo, O. V. Theoretical Insights into Photoinduced Charge Transfer and Catalysis at Oxide Interfaces. *Chem. Rev.* **2013**, *113*, 4496–4565.

(23) Curchod, B. F. E.; Rothlisberger, U.; Tavernelli, I. Trajectory-Based Nonadiabatic Dynamics with Time-Dependent Density Functional Theory. *Chem. Phys. Chem.* **2013**, *14*, 1314–1340.

(24) Rozzi, A. C.; Falke, M. S.; Spallanzani, N.; Rubio, A.; Molinari, E.; Brida, D.; Maiuri, M.; Cerullo, G.; Schramm, H.; Christoffers, J.; Lienau, C. Quantum Coherence Controls the Charge Separation in a Prototypical Artificial Light-Harvesting System. *Nature Communications* **2013**, *4*, 1602.

(25) Eisenmayer, T. J.; Buda, F. Real-Time Simulations of Photoinduced Coherent Charge Transfer and Proton-Coupled Electron Transfer. *ChemPhysChem* **2014**, *15*, 3258–3263.

(26) Menzel, J. P.; de Groot, H. J. M.; Buda, F. Photoinduced Electron Transfer in Donor–Acceptor Complexes: Isotope Effect and Dynamic Symmetry Breaking. *J. Phys. Chem. Lett.* **2019**, *10*, 6504–6511.

(27) Meng, S.; Ren, J.; Kaxiras, E. Natural Dyes Adsorbed on TiO_2 Nanowire for Photovoltaic Applications: Enhanced Light Absorption and Ultrafast Electron Injection. *Nano Lett.* **2008**, *8*, 3266–3272.

(28) Duncan, W. R.; Prezhdo, O. V. Temperature Independence of the Photoinduced Electron Injection in Dye-Sensitized TiO2 Rationalized by Ab Initio Time-Domain Density Functional Theory. *J. Am. Chem. Soc.* **2008**, *130*, 9756–9762.

(29) Meng, S.; Kaxiras, E. Electron and Hole Dynamics in Dye-Sensitized Solar Cells: Influencing Factors and Systematic Trends. *Nano Lett.* **2010**, *10*, 1238–1247.

(30) Kolesov, G.; Grånäs, O.; Hoyt, R.; Vinichenko, D.; Kaxiras, E. Real-Time TD-DFT with Classical Ion Dynamics: Methodology and Applications. *J. Chem. Theory Comput.* **2016**, *12*, 466–476.

(31) Long, R.; Casanova, D.; Fang, W.-H.; Prezhdo, O. V. Donor–Acceptor Interaction Determines the Mechanism of Photoinduced Electron Injection from Graphene Quantum Dots into TiO_2 : π-Stacking Supersedes Covalent Bonding. *J. Am. Chem. Soc.* **2017**, *139*, 2619–2629.

(32) Rego, L. G. C.; Batista, V. S. Quantum Dynamics Simulations of Interfacial Electron Transfer in Sensitized TiO_2 Semiconductors. *J. Am. Chem. Soc.* **2003**, *125*, 7989–7997.

(33) Rego, L. G. C.; Abuabara, S. G.; Batista, V. S. Coherent Optical Control of Electronic Excitations in Functionalized Semiconductor Nanostructures. *Quantum Info. Comput.* **2005**, *5*, 318–334.

(34) Rego, L. G. C.; Abuabara, S. G.; Batista, V. S. Model Study of Coherent Quantum Dynamics of Hole States in Functionalized Semiconductor Nanostructures. *The Journal of Chemical Physics* **2005**, *122*, 154709.

(35) Rego, L. G. C.; Abuabara, S. G.; Batista, V. S. Coherent Control of Tunnelling Dynamics in Functionalized Semiconductor Nanostructures: A Quantum-Control Scenario Based on Stochastic Unitary Pulses. *Journal of Modern Optics* **2006**, *53*, 2519–2532.

(36) Xiao, D.; Martini, L. A.; Snoeberger, R. C.; Crabtree, R. H.; Batista, V. S. Inverse Design and Synthesis of Acac-Coumarin Anchors for Robust TiO2 Sensitization. *J. Am. Chem. Soc.* **2011**, *133*, 9014–9022.

(37) Monti, A.; Negre, C. F. A.; Batista, V. S.; Rego, L. G. C.; de Groot, H. J. M.; Buda, F. Crucial Role of Nuclear Dynamics for Electron Injection in a Dye–Semiconductor Complex. *J. Phys. Chem. Lett.* **2015**, *6*, 2393–2398.

(38) Poddutoori, P. K.; Thomsen, J. M.; Milot, R. L.; Sheehan, S. W.; Negre, C. F. A.; Garapati, V. K. R.; Schmuttenmaer, C. A.; Batista, V. S.; Brudvig, G. W.; van der Est, A. Interfacial Electron Transfer in Photoanodes Based on Phosphorus(V) Porphyrin Sensitizers Co-Deposited on SnO 2 with the Ir(III)Cp* Water Oxidation Precatalyst. *J. Mater. Chem. A* **2015**, *3*, 3868–3879.

(39) McNamara, W. R.; Snoeberger III, R. C.; Li, G.; Richter, C.; Allen, L. J.; Milot, R. L.; Schmuttenmaer, C. A.; Crabtree, R. H.; Brudvig, G. W.; Batista, V. S. Hydroxamate Anchors for Water-Stable Attachment to TiO2 Nanoparticles. *Energy Environ. Sci.* **2009**, *2*, 1173.

(40) Lim, G. N.; Hedström, S.; Jung, K. A.; Smith, P. A. D.; Batista, V. S.; D'Souza, F.; van der Est, A.; Poddutoori, P. K. Interfacial Electron Transfer Followed by Photooxidation in N,N-Bis(p-Anisole)Aminopyridine–Aluminum(III) Porphyrin–Titanium(IV) Oxide Self-Assembled Photoanodes. *J. Phys. Chem. C* **2017**, *121*, 14484–14497.

(41) Lee, S. H.; Regan, K. P.; Hedström, S.; Matula, A. J.; Chaudhuri, S.; Crabtree, R. H.; Batista, V. S.; Schmuttenmaer, C. A.; Brudvig, G. W. Linker Length-Dependent Electron-Injection Dynamics of Trimesitylporphyrins on SnO2 Films. *J. Phys. Chem. C* **2017**, *121*, 22690–22699.

(42) Tichnell, C. R.; Miller, J. N.; Liu, C.; Mukherjee, S.; Jakubikova, E.; McCusker, J. K. Influence of Electrolyte Composition on Ultrafast Interfacial Electron Transfer in Fe-Sensitized TiO2-Based Solar Cells. *J. Phys. Chem. C* **2020**, *124*, 1794–1811.

(43) Shahroosvand, H.; Abaspour, S.; Pashaei, B.; Bideh, B. N. On How Ancillary Ligand Substitution Affects the Charge Carrier Dynamics in Dye-Sensitized Solar Cells. *RSC Adv.* **2018**, *8*, 19465–19469.

(44) Shahroosvand, H.; Abbasi, P.; Bideh, B. N. Dye-Sensitized Solar Cell Based on Novel Star-Shaped Ruthenium Polypyridyl Sensitizer: New Insight into the Relationship between Molecular Designing and Its Outstanding Charge Carrier Dynamics. *ChemistrySelect* **2018**, *3*, 6821–6829.

(45) Abuabara, S. G.; Cady, C. W.; Baxter, J. B.; Schmuttenmaer, C. A.; Crabtree, R. H.; Brudvig, G. W.; Batista, V. S. Ultrafast Photooxidation of Mn(II)−Terpyridine Complexes Covalently Attached to TiO 2 Nanoparticles. *J. Phys. Chem. C* **2007**, *111*, 11982–11990.

(46) Mukherjee, S.; Liu, C.; Jakubikova, E. Comparison of Interfacial Electron Transfer Efficiency in [Fe(Ctpy)2]2+–TiO2 and [Fe(CCNC)2]2+–TiO2 Assemblies: Importance of Conformational Sampling. *J. Phys. Chem. A* **2018**, *122*, 1821–1830.

(47) McNamara, W. R.; Snoeberger, R. C.; Li, G.; Schleicher, J. M.; Cady, C. W.; Poyatos, M.; Schmuttenmaer, C. A.; Crabtree, R. H.; Brudvig, G. W.; Batista, V. S. Acetylacetonate Anchors for Robust Functionalization of TiO 2 Nanoparticles with Mn(II)−Terpyridine Complexes. *J. Am. Chem. Soc.* **2008**, *130*, 14329–14338.

(48) Negre, C. F. A.; Young, K. J.; Oviedo, Ma. B.; Allen, L. J.; Sánchez, C. G.; Jarzembska, K. N.; Benedict, J. B.; Crabtree, R. H.; Coppens, P.; Brudvig, G. W.; Batista, V. S. Photoelectrochemical Hole Injection Revealed in Polyoxotitanate Nanocrystals Functionalized with Organic Adsorbates. *J. Am. Chem. Soc.* **2014**, *136*, 16420–16429.

(49) Hoff, D. A.; Silva, R.; Rego, L. G. C. Subpicosecond Dynamics of Metal-to-Ligand Charge-Transfer Excited States in Solvated [Ru(Bpy)3]2+ Complexes. *J. Phys. Chem. C* **2011**, *115*, 15617–15626.

(50) da Silva, R.; Hoff, D. A.; Rego, L. G. C. Coupled Quantum-Classical Method for Long Range Charge Transfer: Relevance of the Nuclear Motion to the Quantum Electron Dynamics. *J. Phys.: Condens. Matter* **2015**, *27*, 134206.

(51) Hoff, D. A.; da Silva, R.; Rego, L. G. C. Coupled Electron–Hole Quantum Dynamics on D−π–A Dye-Sensitized TiO 2 Semiconductors. *J. Phys. Chem. C* **2012**, *116*, 21169–21178.

(52) Torres, A.; Oliboni, R. S.; Rego, L. G. C. Vibronic and Coherent Effects on Interfacial Electron Transfer Dynamics. *J. Phys. Chem. Lett.* **2015**, *6*, 4927–4935.

(53) da Silva Oliboni, R.; Bortolini, G.; Torres, A.; Rego, L. G. C. A Nonadiabatic Excited State Molecular Mechanics/Extended Hückel Ehrenfest Method. *J. Phys. Chem. C* **2016**, *120*, 27688–27698.
(54) Torres, A.; Prado, L. R.; Bortolini, G.; Rego, L. G. C. Charge Transfer Driven Structural Relaxation in a Push–Pull Azobenzene Dye–Semiconductor Complex. *J. Phys. Chem. Lett.* **2018**, *9*, 5926–5933.
(55) Oliboni, R. S.; Yan, H.; Fan, H.; Abraham, B.; Avenoso, J. P.; Galoppini, E.; Batista, V. S.; Gundlach, L.; Rego, L. G. C. Vibronic Effects in the Ultrafast Interfacial Electron Transfer of Perylene-Sensitized TiO2 Surfaces. *J. Phys. Chem. C* **2019**, *123*, 12599–12607.
(56) Ambrosio, F.; Martsinovich, N.; Troisi, A. What Is the Best Anchoring Group for a Dye in a Dye-Sensitized Solar Cell? *J. Phys. Chem. Lett.* **2012**, *3*, 1531–1535.
(57) Sakai, N.; Mareda, J.; Vauthey, E.; Matile, S. Core-Substituted Naphthalenediimides. *Chem. Commun.* **2010**, *46*, 4225–4237.
(58) Narsaria, A. K.; Ruijter, J. D.; Hamlin, T. A.; Ehlers, A. W.; Guerra, C. F.; Lammertsma, K.; Bickelhaupt, F. M. Performance of TDDFT Vertical Excitation Energies of Core-Substituted Naphthalene Diimides. *Journal of Computational Chemistry* **2020**, *41*, 1448–1455.
(59) Elstner, M.; Porezag, D.; Jungnickel, G.; Elsner, J.; Haugk, M.; Frauenheim, Th.; Suhai, S.; Seifert, G. Self-Consistent-Charge Density-Functional Tight-Binding Method for Simulations of Complex Materials Properties. *Phys. Rev. B* **1998**, *58*, 7260–7268.
(60) Elstner, M.; Frauenheim, T.; Kaxiras, E.; Seifert, G.; Suhai, S. A Self-Consistent Charge Density-Functional Based Tight-Binding Scheme for Large Biomolecules. *physica status solidi (b)* **2000**, *217*, 357–376.
(61) Frauenheim, T.; Seifert, G.; Elsterner, M.; Hajnal, Z.; Jungnickel, G.; Porezag, D.; Suhai, S.; Scholz, R. A Self-Consistent Charge Density-Functional Based Tight-Binding Method for Predictive Materials Simulations in Physics, Chemistry and Biology. *physica status solidi (b)* **2000**, *217*, 41–62.
(62) ADF 2019.3, SCM, Theoretical Chemistry, Vrije Universiteit, Amsterdam, The Netherlands, http://www.scm.com.
(63) Velde, G. te; Bickelhaupt, F. M.; Baerends, E. J.; Fonseca Guerra, C.; van Gisbergen, S. J. A.; Snijders, J. G.; Ziegler, T. Chemistry with ADF. *J. Comput. Chem.* **2001**, *22*, 931–967.
(64) Dolgonos, G.; Aradi, B.; Moreira, N. H.; Frauenheim, T. An Improved Self-Consistent-Charge Density-Functional Tight-Binding (SCC-DFTB) Set of Parameters for Simulation of Bulk and Molecular Systems Involving Titanium. *J. Chem. Theory Comput.* **2010**, *6*, 266–278.
(65) Luttrell, T.; Halpegamage, S.; Tao, J.; Kramer, A.; Sutter, E.; Batzill, M. Why Is Anatase a Better Photocatalyst than Rutile? - Model Studies on Epitaxial TiO 2 Films. *Scientific Reports* **2014**, *4*, 4043.
(66) Rudshteyn, B.; Negre, C. F. A.; Oliboni, R. S.; Monti, A.; Chen, J.; Crabtree, R. H.; Rego, L. G. C.; Batista, V. S. Inferring Protonation States of Hydroxamate Adsorbates on TiO_2 Surfaces. *J. Phys. Chem. C* **2017**, *121*, 11985–11990.
(67) Berendsen, H. J. C.; Postma, J. P. M.; van Gunsteren, W. F.; DiNola, A.; Haak, J. R. Molecular Dynamics with Coupling to an External Bath. *J. Chem. Phys.* **1984**, *81*, 3684–3690.
(68) Alvarez, S. Table of Parameters for Extended Huckel Calculations, Collected by Santiago Alvarez, Universitat de Barcelona (1995). **1995**.
(69) Becke, A. D. A New Mixing of Hartree–Fock and Local Density-functional Theories. *J. Chem. Phys.* **1993**, *98*, 1372–1377.
(70) Lee, C.; Yang, W.; Parr, R. G. Development of the Colle-Salvetti Correlation-Energy Formula into a Functional of the Electron Density. *Phys. Rev. B* **1988**, *37*, 785–789.
(71) Van Lenthe, E.; Baerends, E. J. Optimized Slater-Type Basis Sets for the Elements 1–118. *Journal of Computational Chemistry* **2003**, *24*, 1142–1156.
(72) Pye, C. C.; Ziegler, T. An Implementation of the Conductor-like Screening Model of Solvation within the Amsterdam Density Functional Package. *Theor Chem Acc* **1999**, *101*, 396–408.
(73) Ooyama, Y.; Yamaji, K.; Ohshita, J. Photovoltaic Performances of Type-II Dye-Sensitized Solar Cells Based on Catechol Dye Sensitizers: Retardation of Back-Electron Transfer by PET (Photo-Induced Electron Transfer). *Mater. Chem. Front.* **2017**, *1*, 2243–2255.

(74) Selli, D.; Fazio, G.; Seifert, G.; Di Valentin, C. Water Multilayers on TiO2 (101) Anatase Surface: Assessment of a DFTB-Based Method. *J. Chem. Theory Comput.* **2017**, *13*, 3862–3873.

(75) Aschauer, U. J.; Tilocca, A.; Selloni, A. Ab Initio Simulations of the Structure of Thin Water Layers on Defective Anatase TiO2(101) Surfaces. *International Journal of Quantum Chemistry* **2015**, *115*, 1250–1257.

4.A Appendix

4A.1 Extended Hückel parameter optimization

In the quantum dynamics calculations, the correct energetic values of the involved orbitals are crucial, since they determine the thermodynamic driving force as well as the time evolution of the electronic wave packets. They are obtained using the tight binding Hamiltonian based on Extended Hückel theory that was described in chapter 2. To obtain reliable results, we need to optimize the semi-empirical parameters defining the matrix elements of the Extended Hückel Hamiltonian in such a way that they reproduce experimental values. As there is only limited experimental information on some of the investigated molecules, an alternative to experimental values is needed for parameter optimization. Here, we use ΔSCF[1,2] values obtained in implicit solvation to obtain the ionization potential that is related to the HOMO via the Koopmans theorem.[3] Thereby, a geometry optimization of the neutral species was performed, as well as an unrestricted calculation on this same geometry with one electron removed. The energy difference between these two SCF calculations is then a reasonable estimate of the experimental oxidation potential. These values were calculated with the ADF program by SCM (Software for Chemistry and Materials)[4,5] at the DFT/B3LYP[6–8] level using a Double Zeta with one Polarization Function (DZP) basis set[9] and D3 dispersion corrections with BJ-damping[10,11] within COSMO[12] implicit water solvation. This combination was chosen, since the ΔSCF results in the corresponding implicit solvation agree reasonably well with available experimental oxidation potentials (see table 4A.1).

Table 4A.1: Experimental oxidation potential, ΔSCF estimate using B3LYP/DZP, D3-BJ and COSMO solvation of the solvent used in the experiment and COSMO water.

Molecule	Solvent used in experiment	ΔSCF in experimental solvent [eV]	Experimental Oxidation Potential [V]	ΔSCF in COSMO water [eV]
Catechol	Acetonitrile	-5.86	-5.83[13]	-5.79
Benzoic acid	Water	-7.07	-	-7.07
Benzhydroxamic acid	Water	-6.74	-	-6.74
NDI	Dichloromethane (DCM)	-7.01	-7.07[14]	-6.94
NDI_2OEt	DCM	-6.31	-6.16[14]	-6.05
NDI_2NHEt	DCM	-5.45	-5.35[14]	-5.20
NDI_NHEt_OEt	DCM	-5.81	-5.75[14]	-5.55

For the NDI based dyes, the LUMO target energy was obtained by using the before mentioned ΔSCF value for the HOMO energy and adding the TD-DFT excitation energy obtained on the same geometry with the same settings. These values agree reasonably well with experimental values for several tested NDIs (see table 4A.2). Recently, also Narsaria *et al.* showed that B3LYP excitation energies for NDIs have a strong correlation with experimental excitation energies.[15]

Table 4A.2: Experimental oxidation potential, ΔSCF estimate using B3LYP/DZP, D3-BJ and COSMO solvation of the solvent used in the experiment, ΔSCF + TDDFT excitation energy estimate, experimental reduction potential. Values differing more than 0.2 eV marked in bold.

Molecule	Solvent used in experiment	ΔSCF in experim. solvent [eV]	Experim. Oxidation Potential [V]	ΔSCF + TDDFT Excitation energy (in brackets)	Experim. Reduction Potential [V]
Catechol	Acetonitrile	-5.86	-5.83[13]	**-0.93 (4.93)**	**-1.65**[13]
NDI	DCM	-7.01	-7.07[14]	-3.91 (3.10)	-4.01[14]
NDI_2OEt	DCM	-6.31	-6.16[14]	-3.77 (2.55)	-3.82[14]
NDI_ 2NHEt	DCM	-5.45	-5.35[14]	-3.52 (1.94)	-3.56[14]
NDI_ NHEt_OEt	DCM	-5.81	-5.75[14]	-3.62 (2.20)	-3.75[14]

Unfortunately, for the benzene based anchoring groups, this method does not give an accurate estimate and thus a different approach has been taken. The ΔSCF value still describes the experimental oxidation potential reasonably well and therefore is still taken as a reference for the HOMO energy. For the LUMO energy, the ΔSCF value plus the experimental onset of the first UV-Vis absorption peak is taken as reference, since also in experiments, difficult redox potentials are often estimated using this onset value and subtracting / adding it to the more easily obtained redox potential (reduction / oxidation potential).[13,14]

To summarize, the target energies for the frontier orbitals are obtained as follows: For all molecules, the ΔSCF values in water (COSMO) were used as HOMO target value. For the anchoring molecules catechol, benzoic acid and benzohydroxamic acid, the experimental first absorption peak onset energy was added to the ΔSCF value to obtain an estimate for the LUMO energy. For the NDI-derived molecules, the TDDFT excitation energies in COSMO using B3LYP/DZP for the excitation with the largest oscillator strength (here always the HOMO-LUMO excitation) were added to the ΔSCF values as an estimate for the LUMO energy. The values are reported in table 4A.3.

Optimization of the parameters was performed on the free dye and anchor molecules: they were optimized in their neutral (thus protonated) form before dissociative adsorption on the TiO_2 surface. Since the nuclear dynamics were performed using SCC-DFTB[16–18] with the tiorg-0-1 parameter set[19], the geometry optimization was performed with the same settings. Since the conduction band edge of the TiO_2 with the Extended Hückel Hamiltonian is at -10.00 eV and the experimental value for the anatase conduction band edge is at approximately -4.05 eV[20], the target values of the frontier orbitals of the molecules are shifted by -5.95 eV to give the correct energetic alignment. The optimization procedure itself was performed using a genetic algorithm and cost function that are described elsewhere.[21]

Table 4A.3: Target energies for HOMO (ΔSCF) and LUMO (either ΔSCF + TDDFT excitation energy or ΔSCF + experimental absorption peak onset energy).

Molecule	**Target HOMO [eV]**	**Target LUMO [eV]**	
	ΔSCF (water)	ΔSCF + TDDFT excitation energy in water (brackets)	ΔSCF + experimental absorption peak onset (brackets)
Catechol	-5.79		-1.61 (4.18[13])
Benzoic Acid	-7.07		-2.77 (~4.3[22])
Benzohydroxamic Acid	-6.74		-2.44 (~4.3[22])
2OEt-NDI	-6.05	-3.56 (2.50)	
Cat-NDI	-5.55	-3.50 (2.05)	
Ben-NDI	-6.06	-3.88 (2.18)	
Hyd-NDI	-6.04	-3.88 (2.16)	

Only HOMO and LUMO energies were used as targets. In table 4A.4 we compare the HOMO and LUMO energies obtained with standard parameters, the target values and the energies obtained with the optimized parameters.

Table 4A.4: HOMO/LUMO energies for the different molecules obtained with standard Hückel parameters, target values generated above with linear shift of -5.95 eV and obtained with optimized Hückel parameters.

Molecule	**Standard Hückel Parameters [eV]**		**Target values [eV]**		**Optimized Hückel parameters [eV]**	
	HOMO	LUMO	HOMO	LUMO	HOMO	LUMO
Catechol	-12.20	-8.17	-11.74	-7.56	-11.75	-7.55
Benzoic Acid	-12.81	-9.62	-13.02	-8.72	-13.02	-8.72
Benzohydroxamic Acid	-12.69	-9.43	-12.69	-8.39	-12.70	-8.39
2OEt-NDI	-12.14	-10.63	-12.00	-9.51	-12.00	-9.52
Cat-NDI	-11.96	-10.76	-11.50	-9.45	-11.50	-9.45
Ben-NDI	-12.10	-10.84	-12.01	-9.83	-12.01	-9.83
Hyd-NDI	-12.07	-10.83	-11.99	-9.83	-11.96	-9.81

The spatial distribution of the frontier orbitals was checked against their respective B3LYP counter parts to exclude unphysical orbitals. For the anchoring molecules, this was extended to HOMO-1 and LUMO+1 as well, since their high symmetry results in several near degenerate states that might mix and cross due to changing nuclear geometries. In tables 4A.5 and 4A.6, the spatial distribution of the frontier orbitals using B3LYP/COSMO and Extended Hückel using the optimized parameters are shown for the anchoring molecules and dyes. The optimized parameters give frontier orbital energies as well as spatial distributions that are very close to the B3LYP results.

Table 4A.5: Spatial distribution of HOMO-1, HOMO, LUMO and LUMO+1 for the three anchoring molecules, using B3LYP and the Extended Hückel method with optimized parameters

Molecule /Method	HOMO-1	HOMO	LUMO	LUMO+1
Catechol				
B3LYP		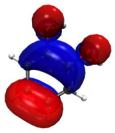	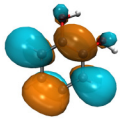	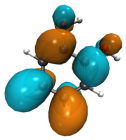
Extended Hückel Optimized	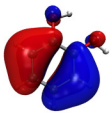	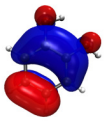	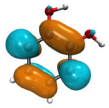	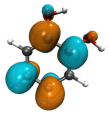
Benzoic Acid				
B3LYP	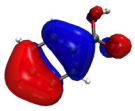	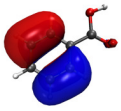	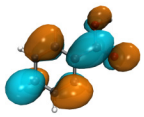	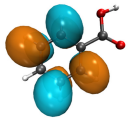
Extended Hückel Optimized	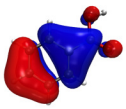	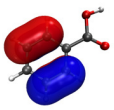	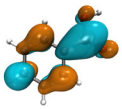	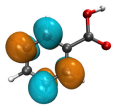
Benzohydroxamic Acid				
B3LYP	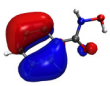	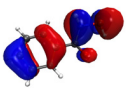	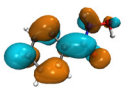	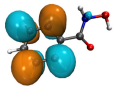
Extended Hückel Optimized	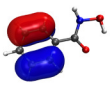	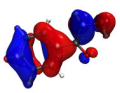	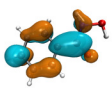	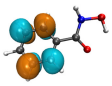

Table 4A.6: Spatial distribution of HOMO and LUMO for the NDI-based dyes, using B3LYP and the Extended Hückel method with optimized parameters

	HOMO		***LUMO***	
	B3LYP	*Extended Hückel*	*B3LYP*	*Extended Hückel*
2OEt-NDI	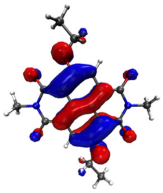	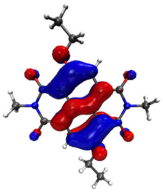	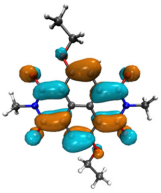	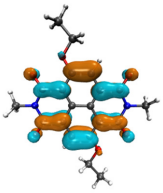
Cat-NDI	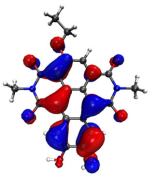	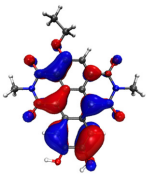	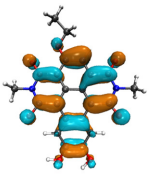	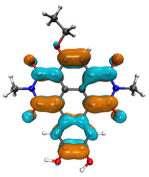
Ben-NDI	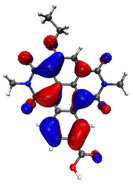	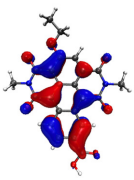	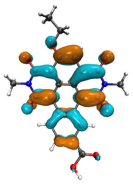	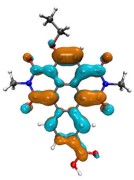
Hyd-NDI	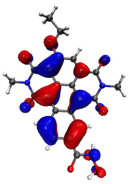	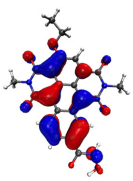	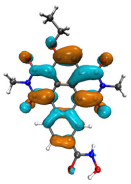	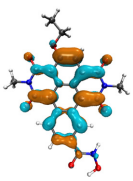

In figure 4A.1, the energetic alignment of the frontier orbitals of all optimized molecules are shown in comparison to the TiO_2 conduction band edge. As can be seen, all molecules have sufficient driving force to inject into the conduction band. The benzene derived anchoring groups have significantly higher LUMO energies than the NDI derived dyes. The carboxylic acid and hydroxamic acid-based core extended ethoxy NDIs have very similar LUMO energies close to the conduction band edge, while the catechol increases both the HOMO and LUMO energy values of the NDI in comparison to the other two anchoring groups.

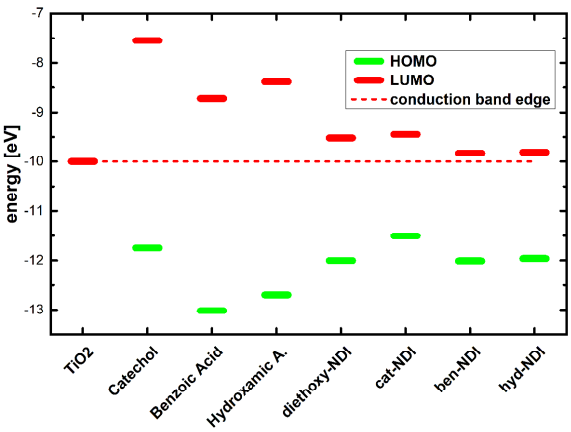

Figure 4A.1. HOMO and LUMO energies of the investigated anchoring molecules and dyes in comparison to the conduction band edge of anatase (dashed line) obtained with the Extended Hückel method using the optimized parameters.

Of course, this alignment might change during the attachment of the molecules on the TiO_2 surface and also during the dynamics. In figure 4A.2, the Partial Density of States (PDOS) of TiO_2 and the investigated anchoring molecules from the full photoanode system, with anchoring molecules attached to the electrode and explicit solvent is shown for comparison. All three anchoring molecules have a LUMO energy that is well within the conduction band of the TiO_2. Therefore, there is a driving force to inject a photoexcited electron into the conduction band. Catechol has the highest LUMO, followed by the benzohydroxamic acid and then the benzoic acid. The benzoic acid has a low amount of state density below the LUMO that comes from conduction band states that extend over the carboxylic acids' oxygens. This overlap might also explain the initial ultrafast injection of the benzoic acid, where the electron wave packet rapidly expands from the fragment LUMO onto states involving the TiO_2. In general, the HOMO – LUMO gap of the anchoring molecules is quite high and the LUMO well above the conduction band edge.

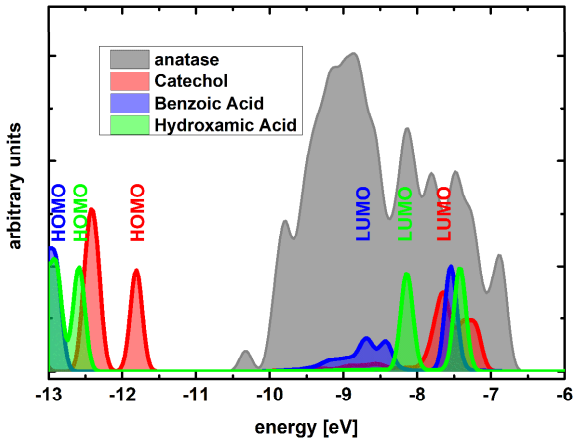

Figure 4A.2. Partial Densities of States (PDOS) in band gap and conduction band of the TiO_2 electrode (grey) and the adsorbed anchoring molecules catechol (red), benzoic acid (blue) and benzohydroxamic acid (green). The TiO_2 PDOS has been divided by 5 for easier comparison. Frontier orbitals are marked.

In figure 4A.3, the PDOS of the core extended ethoxy NDI molecules is shown in comparison to the TiO_2. HOMO-LUMO gaps are significantly lower than for the respective anchoring molecules. Cat-NDI has the highest LUMO energy, above the conduction band edge. Ben-NDI and Hyd-NDI show very similar PDOS, with their LUMOs slightly above the conduction band edge.

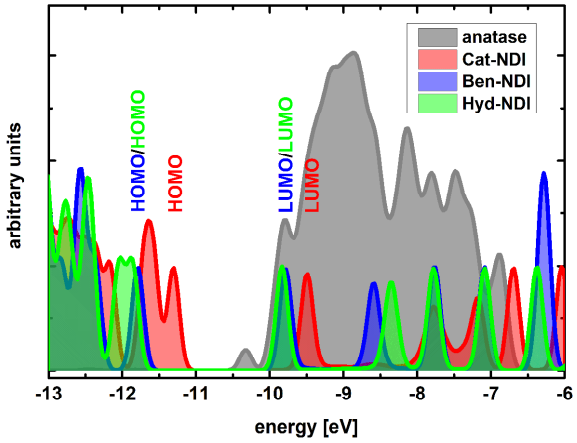

Figure 4A.3. Partial Densities of States (PDOS) in band gap and conduction band of the TiO_2 electrode (grey) and the adsorbed anchoring molecules cat-NDI (red), ben-NDI (blue) and hyd-NDI (green). The TiO_2 PDOS has been divided by 5 for easier comparison. Frontier orbitals are marked.

Here, the driving force is significantly lower than for the anchoring molecules, which is reflected in their significantly lower injection rates. However, the HOMO-LUMO gap lies for all three NDI molecules well in the visible light range and alignment seems favorable.

4A.2 Influence of dihedral angle on electron injection

In some of the ETD simulations, the observed delay in the injection can be tightly associated to the dihedral angle between the anchoring group and the aromatic system of the organic molecule. One such example is shown in figure 4A.4, where electron injection from benzohydroxamic acid is shown.

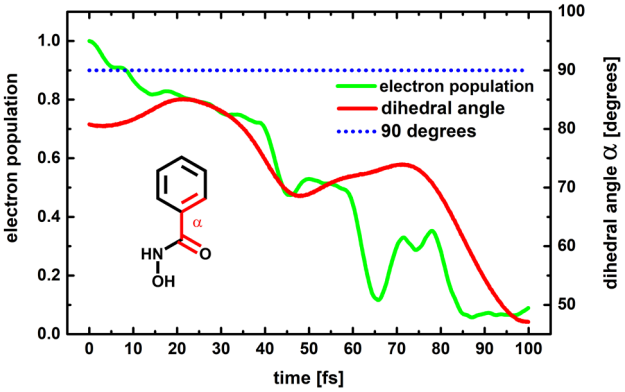

Figure 4A.4. Electron population on ben-NDI over time (green) in comparison to dihedral angle α (red) shown in the inlet structure. The dotted blue line corresponds to 90 degrees. Electron injection is hindered when the dihedral angle is close to 90 degrees, breaking conjugation.

A simulation with delayed injection was chosen and compared to the associated change in dihedral angle shown in the inset chemical structure. Injection is hindered when the angle approaches 90 degrees, breaking possible conjugation between the benzene group and the hydroxamate subsystem.

In figure 4A.5, an example is given from the ben-NDI case. The initial electron injection is fast, but at around 150 fs is stagnating, while the dihedral angle approaches 90 degrees with the aromatic system and anchoring group perpendicular to each other. For about 250 fs, the injection process is halted and only starts again

when the dihedral angle leaves the region around 90 degrees, opening a channel via the anchoring group.

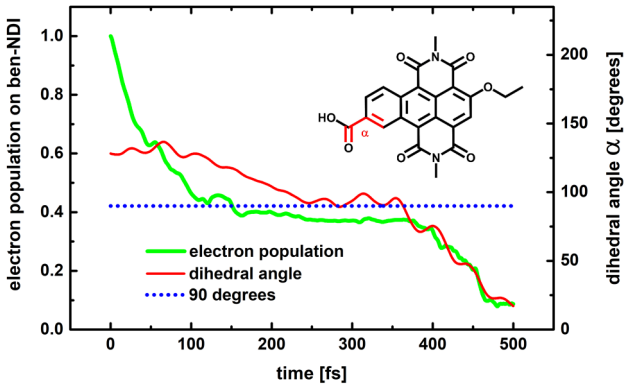

Figure 4A.5. Electron population on ben-NDI over time (green) in comparison to dihedral angle (red) shown in the inlet structure. The dotted blue line corresponds to 90 degrees. Electron injection is hindered when the dihedral angle is close to 90 degrees, breaking conjugation.

4A.3 Resonance coupling in the electron transfer process

As shown before, the nuclear geometries can allow or prohibit electron flow from the photoexcited dye towards the electrode. However, the nuclear motion itself can also be used by the electron for a rapid injection by taking advantage of resonant coupling. Whereas the electronic system is not able to activate nuclear modes and slow down the nuclear motion in the sense of coherent conversion from reactant to product state, it can use present modes available through the incoherent thermal noise for a nonadiabatic population transfer. As the LUMO of the dye molecules lays energetically within the conduction band of the TiO_2 electrode, the energy difference between electronic states is very small and a myriad of different states can couple to another. This leads to a very rich selection of modes that the electronic system can couple to in the region $w/2p < 1000\ cm^{-1}$. Both, the electronic frequencies as well as the total nuclear vibrational density of states (VDOS) of a single electron injection trajectory of the photoexcited hyd-NDI molecule, are given in figure 4A.6. Water molecules are omitted from the VDOS for clarity. As is clear from the figure, most electronic frequencies (red) lie in the region $w/2p < 1000\ cm^{-1}$, where a large variety of nuclear modes (blue) is available.

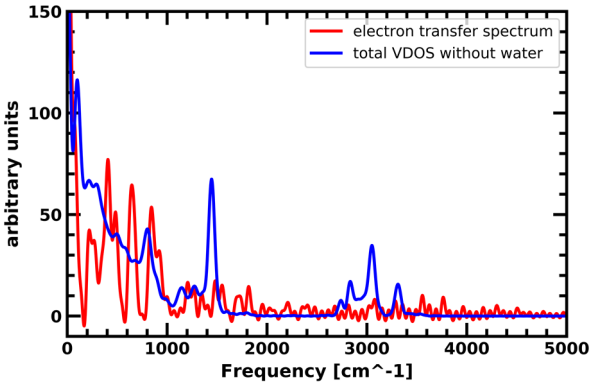

Figure 4A.6. Electron transfer frequencies (red) and total VDOS (blue) of a single trajectory of electron injection from photoexcited hydNDI with explicit water. The water molecules are removed from the VDOS for clarity. Notable are the large peaks in the electron transfer frequencies at low wavenumbers and the abundance of nuclear modes in the same region. A gaussian window function with a sigma value of 5 was used to reduce noise.

Over the course of the injection process, the electronic system can therefore couple to several nuclear modes, with some modes becoming more pronounced over the trajectory and others whose role diminishes. We note that this huge variety of possible pathways also leads to a significant speed-up of the conversion, especially within the electrode, since the high density of electronic states in the conduction band lead to a quick conversion to low lying states. In this system, the role of resonant coupling plays therefore an important role, but which exact modes couple to this process is of less relevance since there is a wide collection of modes available, that have very similar frequencies: there will always be a mode of correct frequency available.

Nevertheless, we show an example of resonant coupling between the electronic system and a specific nuclear mode below in figure 4A.7, that becomes so dominant in a part of the trajectory, that it can clearly be associated to the conversion process. The electronic frequencies and VDOS of the dihedral angle shown in the inset are given for the time 150-250 fs, where the coupling is most pronounced.

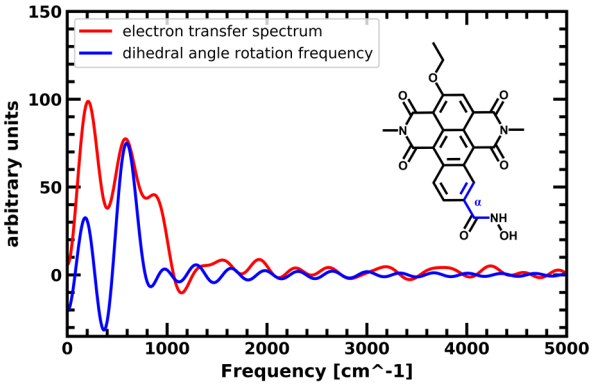

Figure 4A.7. Electron transfer frequency (red) and frequencies of the dihedral angle rotation (blue) marked in the inlet for the same trajectory as above between 150 and 250 fs. There is a clear resonance between the nuclear mode and the electron transfer frequencies with a peak at around 570 cm^{-1}. A gaussian window function with a sigma of 1 was used to reduce noise.

4A.4 Photoinduced electron injection – Catechol

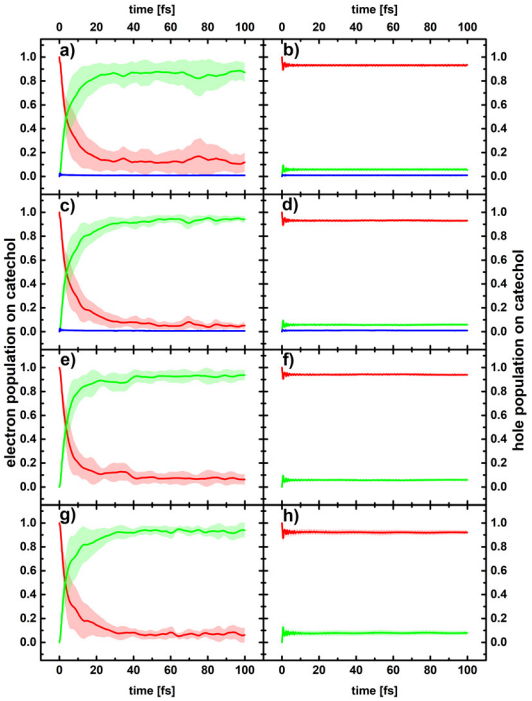

Figure 4A.8. Electron population (left panels) and hole population (right panels) on catechol (red), TiO_2 (green) and water (blue) averaged over 15 ETDs on
a)/b) static geometries,
c)/d) nuclear trajectories with explicit solvation,
e)/f) nuclear trajectories with explicit water removed,
g)/h) nuclear trajectories without water.
The bold lines denote the mean value, the shaded areas represent the standard deviation centered on the mean value.

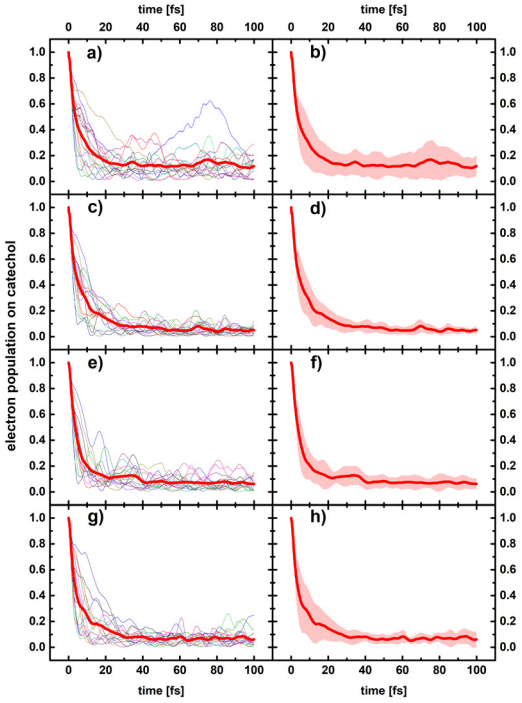

Figure 4A.9. Electron population on catechol. The left panels show the 15 single ETD runs in narrow lines, the resulting mean average in bold red; the right panels give this same mean average in bold red with the shaded areas representing the standard deviation. Results obtained on
a/b) static geometries,
c/d) nuclear trajectories with explicit water,
e/f) nuclear trajectories with water removed,
g/h) nuclear trajectories without water.

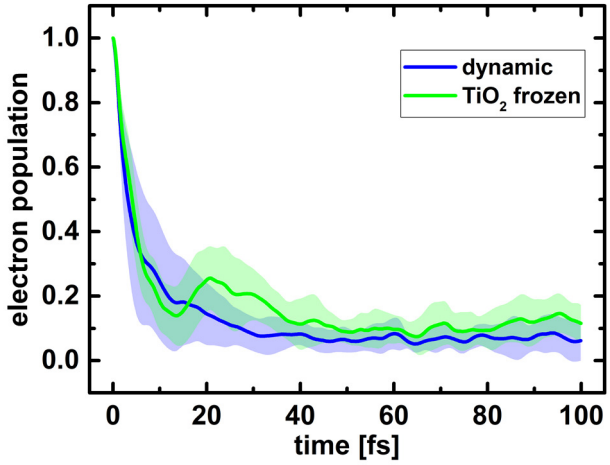

Figure 4A.10. Electron population on catechol averaged over 15 ETDs without explicit solvation allowing for TiO_2 nuclear dynamics (blue) and when freezing the TiO_2 electrode (green). The bold lines represent the mean value, the shaded areas the standard deviation.

4A.5 Photoinduced electron injection – Benzoic acid

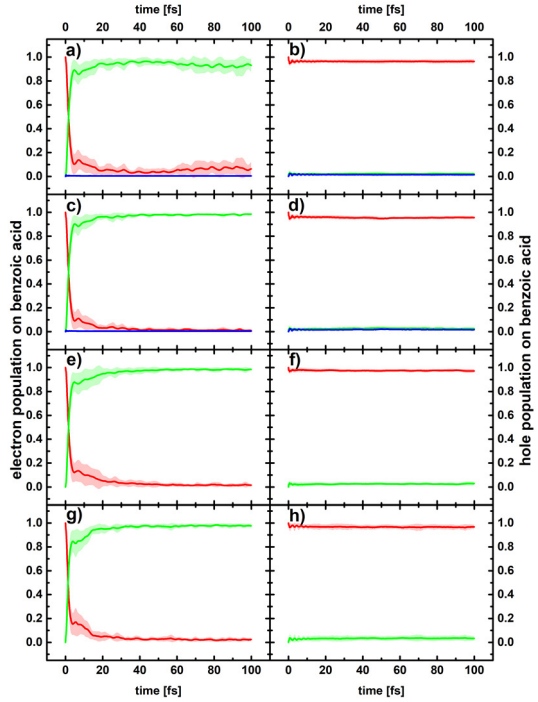

Figure 4A.11. Electron population (left panels) and hole population (right panels) on benzoic acid (red), TiO_2 (green) and water (blue) averaged over 15 ETDs on
a)/b) static geometries,
c)/d) nuclear trajectories with explicit solvation,
e)/f) nuclear trajectories with explicit water removed,
g)/h) nuclear trajectories without water.
The bold lines denote the mean value, the shaded areas represent the standard deviation centered on the mean value.

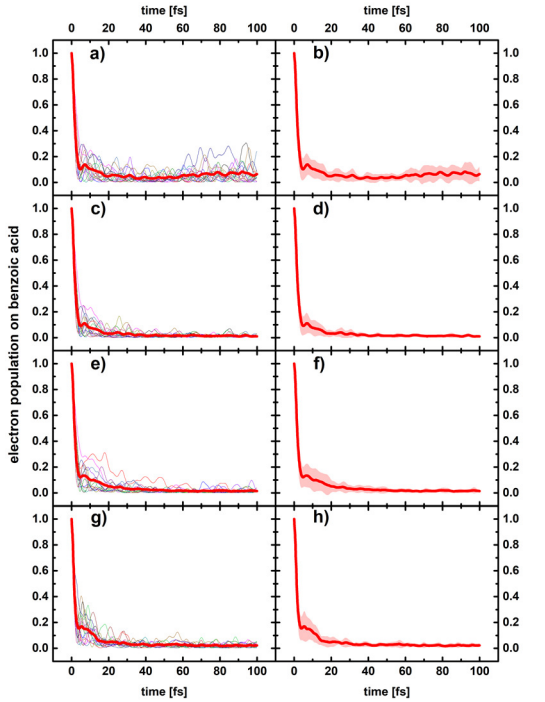

Figure 4A.12. Electron population on benzoic acid. The left panels show the 15 single ETD runs in narrow lines, the resulting mean average in bold red, the right panels give this same mean average in bold red with the shaded areas representing the standard deviation. Results obtained on
a/b) static geometries,
c/d) nuclear trajectories with explicit water,
e/f) nuclear trajectories with water removed,

4A.6 Photoinduced electron injection – Benzohydroxamic acid

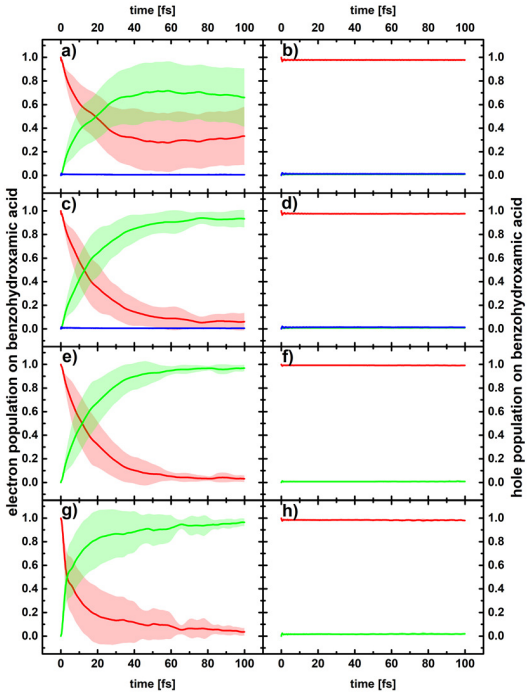

Figure 4A.13. Electron population (left panels) and hole population (right panels) on benzohydroxamic acid (red), TiO_2 (green) and water (blue) averaged over 15 ETDs on
a)/b) static geometries,
c)/d) nuclear trajectories with explicit solvation,
e)/f) nuclear trajectories with explicit water removed,
g)/h) nuclear trajectories without water.
The bold lines denote the mean value, the shaded areas represent the standard deviation centered on the mean value.

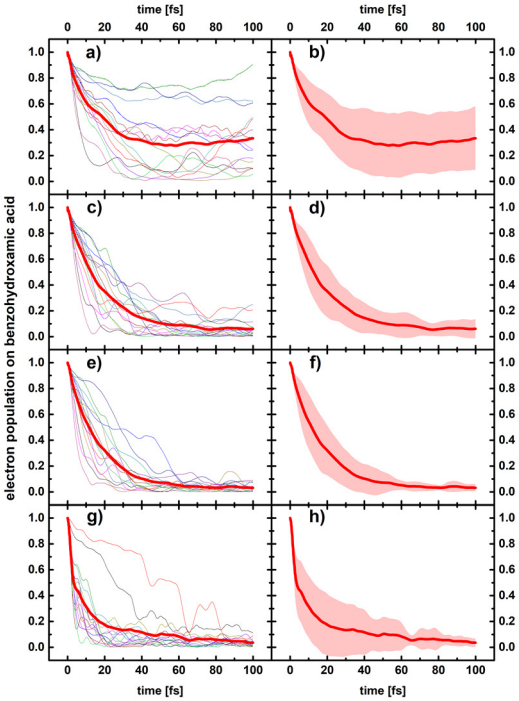

Figure 4A.14. Electron population on benzohydroxamic acid. The left panels show the 15 single ETD runs in narrow lines, the resulting mean average in bold red, the right panels give this same mean average in bold red with the shaded areas representing the standard deviation. Results obtained on
a/b) static geometries,
c/d) nuclear trajectories with explicit water,
e/f) nuclear trajectories with water removed,
g/h) nuclear trajectories without water.

4A.7 Photoinduced electron injection – Cat-NDI

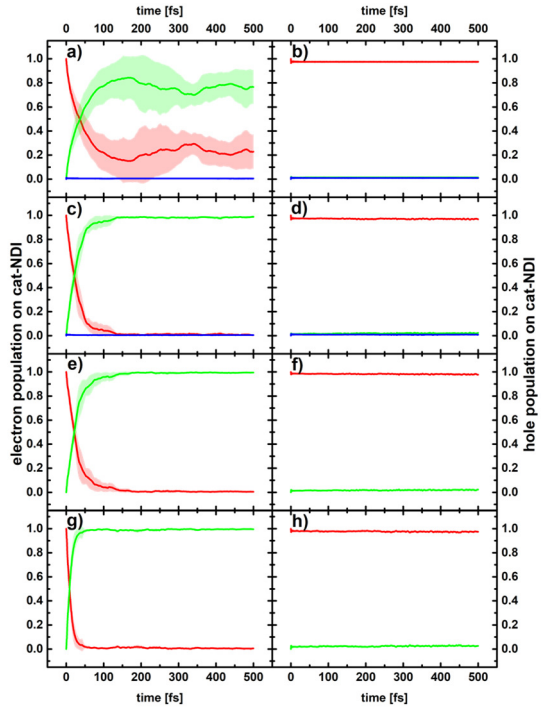

Figure 4A.15. Electron population (left panels) and hole population (right panels) on cat-NDI (red), TiO_2 (green) and water (blue) averaged over 5 ETDs on
a)/b) static geometries,
c)/d) nuclear trajectories with explicit solvation,
e)/f) nuclear trajectories with explicit water removed,
g)/h) nuclear trajectories without water. The bold lines denote the mean value, the shaded areas represent the standard deviation centered on the mean value.

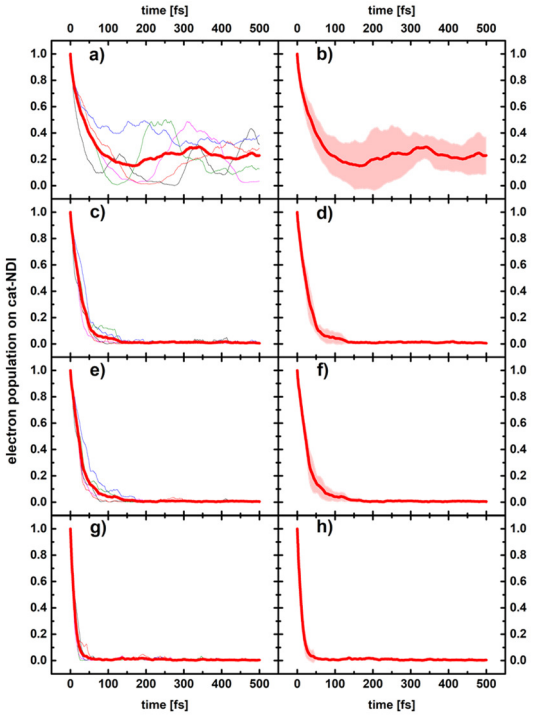

Figure 4A.16. Electron population on cat-NDI. The left panels show the 5 single ETD runs in narrow lines, the resulting mean average in bold red, the right panels give this same mean average in bold red with the shaded areas representing the standard deviation. Results obtained on
a/b) static geometries,
c/d) nuclear trajectories with explicit water,
e/f) nuclear trajectories with water removed,
g/h) nuclear trajectories without water.

4A.8 Photoinduced electron injection – Ben-NDI

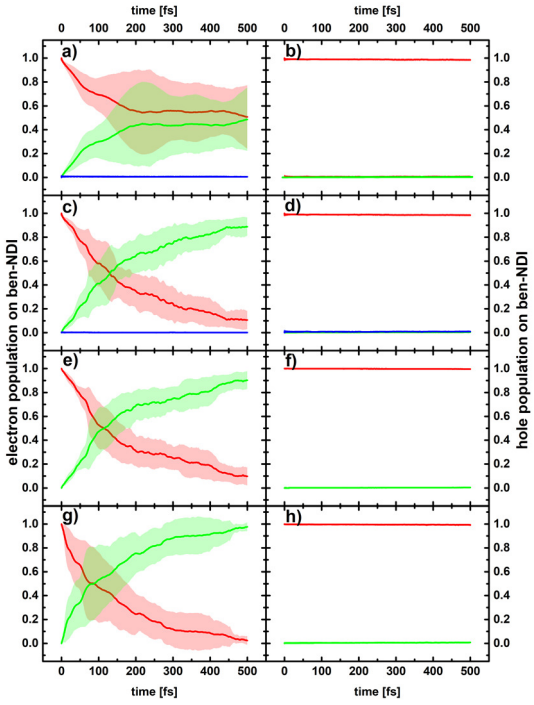

Figure 4A.17. Electron population (left panels) and hole population (right panels) on ben-NDI (red), TiO_2 (green) and water (blue) averaged over 5 ETDs on
a)/b) static geometries,
c)/d) nuclear trajectories with explicit solvation,
e)/f) nuclear trajectories with explicit water removed,
g)/h) nuclear trajectories without water. The bold lines denote the mean value, the shaded areas represent the standard deviation centered on the mean value.

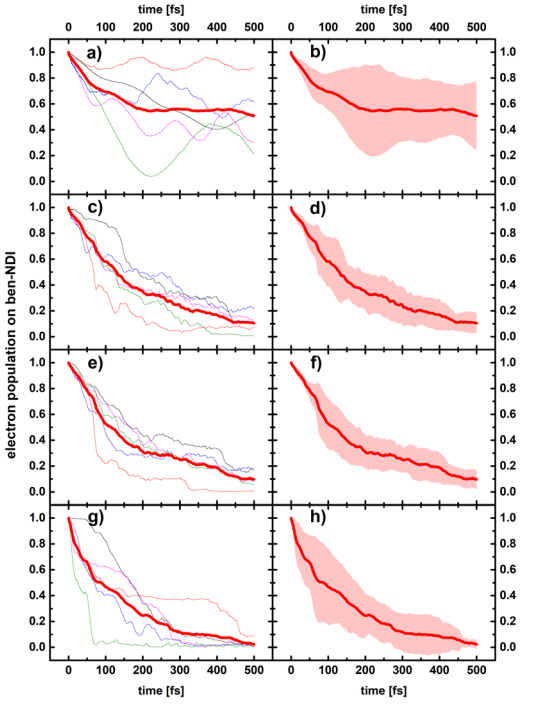

Figure 4A.18. Electron population on ben-NDI. The left panels show the 5 single ETD runs in narrow lines, the resulting mean average in bold red, the right panels give this same mean average in bold red with the shaded areas representing the standard deviation. Results obtained on
a/b) static geometries,
c/d) nuclear trajectories with explicit water,
e/f) nuclear trajectories with water removed,
g/h) nuclear trajectories without water.

4A.9 Photoinduced electron injection – Hyd-NDI

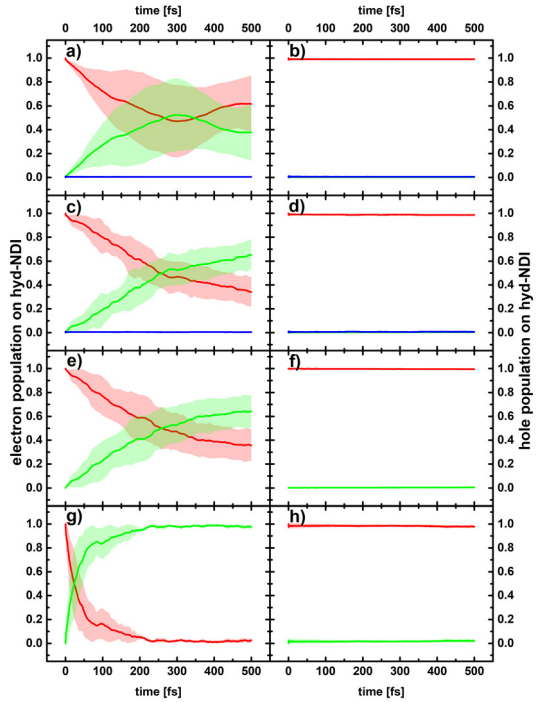

Figure 4A.19. Electron population (left panels) and hole population (right panels) on hyd-NDI (red), TiO_2 (green) and water (blue) averaged over 5 ETDs on
a)/b) static geometries,
c)/d) nuclear trajectories with explicit solvation,
e)/f) nuclear trajectories with explicit water removed,
g)/h) nuclear trajectories without water.
The bold lines denote the mean value, the shaded areas represent the standard deviation centered on the mean value.

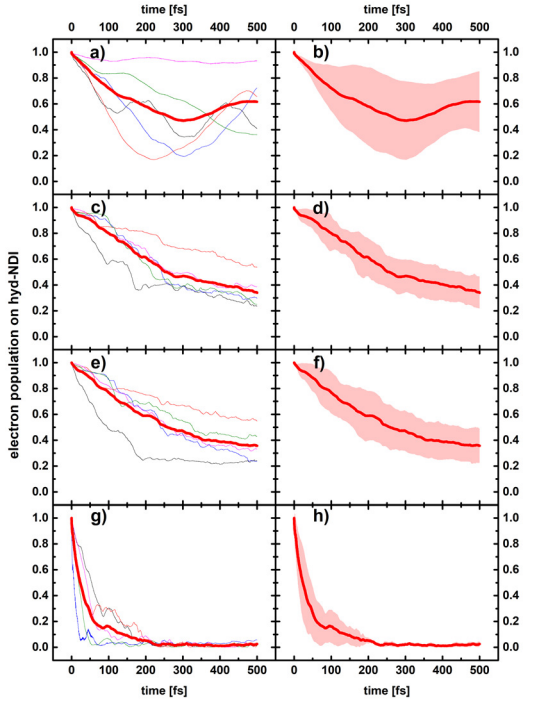

Figure 4A.20. Electron population on hyd-NDI. The left panels show the 5 single ETD runs in narrow lines, the resulting mean average in bold red, the right panels give this same mean average in bold red with the shaded areas representing the standard deviation. Results obtained on
a/b) static geometries,
c/d) nuclear trajectories with explicit water,
e/f) nuclear trajectories with water removed,
g/h) nuclear trajectories without water.

4A.10 References

(1) Gunnarsson, O.; Lundqvist, B. I. Exchange and Correlation in Atoms, Molecules, and Solids by the Spin-Density-Functional Formalism. *Phys. Rev. B* **1976**, *13* (10), 4274–4298.

(2) Jones, R. O.; Gunnarsson, O. The Density Functional Formalism, Its Applications and Prospects. *Rev. Mod. Phys.* **1989**, *61* (3), 689–746.

(3) Koopmans, T. Über die Zuordnung von Wellenfunktionen und Eigenwerten zu den Einzelnen Elektronen Eines Atoms. *Physica* **1934**, *1* (1), 104–113.

(4) Velde, G. te; Bickelhaupt, F. M.; Baerends, E. J.; Fonseca Guerra, C.; van Gisbergen, S. J. A.; Snijders, J. G.; Ziegler, T. Chemistry with ADF. *J. Comput. Chem.* **2001**, *22* (9), 931–967.

(5) ADF 2019.3, SCM, Theoretical Chemistry, Vrije Universiteit, Amsterdam, The Netherlands, http://www.scm.com. .

(6) Becke, A. D. Density-Functional Exchange-Energy Approximation with Correct Asymptotic Behavior. *Phys. Rev. A* **1988**, *38* (6), 3098–3100.

(7) Becke, A. D. A New Mixing of Hartree–Fock and Local Density-functional Theories. *J. Chem. Phys.* **1993**, *98* (2), 1372–1377.

(8) Lee, C.; Yang, W.; Parr, R. G. Development of the Colle-Salvetti Correlation-Energy Formula into a Functional of the Electron Density. *Phys. Rev. B* **1988**, *37* (2), 785–789.

(9) Van Lenthe, E.; Baerends, E. J. Optimized Slater-Type Basis Sets for the Elements 1–118. *Journal of Computational Chemistry* **2003**, *24*, 1142–1156.

(10) Grimme, S.; Antony, J.; Ehrlich, S.; Krieg, H. A Consistent and Accurate Ab Initio Parametrization of Density Functional Dispersion Correction (DFT-D) for the 94 Elements H-Pu. *J. Chem. Phys.* **2010**, *132* (15), 154104.

(11) Grimme, S.; Ehrlich, S.; Goerigk, L. Effect of the Damping Function in Dispersion Corrected Density Functional Theory. *Journal of Computational Chemistry* **2011**, *32* (7), 1456–1465.

(12) Pye, C. C.; Ziegler, T. An Implementation of the Conductor-like Screening Model of Solvation within the Amsterdam Density Functional Package. *Theor Chem Acc* **1999**, *101* (6), 396–408.

(13) Ooyama, Y.; Yamaji, K.; Ohshita, J. Photovoltaic Performances of Type-II Dye-Sensitized Solar Cells Based on Catechol Dye Sensitizers: Retardation of Back-Electron Transfer by PET (Photo-Induced Electron Transfer). *Mater. Chem. Front.* **2017**, *1* (11), 2243–2255.

(14) Sakai, N.; Mareda, J.; Vauthey, E.; Matile, S. Core-Substituted Naphthalenediimides. *Chem. Commun.* **2010**, *46* (24), 4225–4237.

(15) Narsaria, A. K.; Ruijter, J. D.; Hamlin, T. A.; Ehlers, A. W.; Guerra, C. F.; Lammertsma, K.; Bickelhaupt, F. M. Performance of TDDFT Vertical Excitation Energies of Core-Substituted Naphthalene Diimides. *Journal of Computational Chemistry* **2020**, *41* (15), 1448–1455.

(16) Elstner, M.; Porezag, D.; Jungnickel, G.; Elsner, J.; Haugk, M.; Frauenheim, Th.; Suhai, S.; Seifert, G. Self-Consistent-Charge Density-Functional Tight-Binding Method for Simulations of Complex Materials Properties. *Phys. Rev. B* **1998**, *58* (11), 7260–7268.

(17) Elstner, M.; Frauenheim, T.; Kaxiras, E.; Seifert, G.; Suhai, S. A Self-Consistent Charge Density-Functional Based Tight-Binding Scheme for Large Biomolecules. *physica status solidi (b)* **2000**, *217* (1), 357–376.

(18) Frauenheim, T.; Seifert, G.; Elsterner, M.; Hajnal, Z.; Jungnickel, G.; Porezag, D.; Suhai, S.; Scholz, R. A Self-Consistent Charge Density-Functional Based Tight-Binding Method for Predictive Materials Simulations in Physics, Chemistry and Biology. *physica status solidi (b)* **2000**, *217* (1), 41–62.

(19) Dolgonos, G.; Aradi, B.; Moreira, N. H.; Frauenheim, T. An Improved Self-Consistent-Charge Density-Functional Tight-Binding (SCC-DFTB) Set of Parameters for Simulation of Bulk and Molecular Systems Involving Titanium. *J. Chem. Theory Comput.* **2010**, *6* (1), 266–278.

(20) Fujisawa, J.; Eda, T.; Hanaya, M. Comparative Study of Conduction-Band and Valence-Band Edges of TiO2, SrTiO3, and BaTiO3 by Ionization Potential Measurements. *Chemical Physics Letters* **2017**, *685*, 23–26.

(21) Monti, A.; Negre, C. F. A.; Batista, V. S.; Rego, L. G. C.; de Groot, H. J. M.; Buda, F. Crucial Role of Nuclear Dynamics for Electron Injection in a Dye–Semiconductor Complex. *J. Phys. Chem. Lett.* **2015**, *6* (12), 2393–2398.

(22) Glorius, M.; Moll, H.; Bernhard, G. Complexation of Uranium(VI) with Aromatic Acids in Aqueous Solution – a Comparison of Hydroxamic Acids and Benzoic Acid. *Radiochimica Acta* **2007**, *95* (3), 151–157.